Nano-FTIR Investigation of the CM Chondrite Allan Hills 83100

J. M. Young[1], T. D. Glotch[1], M. Yesiltas[2], V. E. Hamilton[3], L. B. Breitenfeld[1], H. A. Bechtel[4], S. N. Gilbert Corder[4], Z. Yao[5]

[1] Department of Geosciences, Stony Brook University, Stony Brook, NY, USA

[2] Faculty of Aeronautics and Space Sciences, Kirklareli University, Kirklareli, Turkey

[3] Southwest Research Institute, Boulder, CO, USA

[4] Advanced Light Source, Lawrence Berkeley National Laboratory, Berkeley, CA, USA

[5] Department of Physics and Astronomy, Stony Brook University, Stony Brook, NY, USA

Corresponding author: Timothy D. Glotch (timothy.glotch@stonybrook.edu)

Key Points:

- Nano-FTIR spectroscopy provides extremely fine-scale (~20 nm) spatially resolved mineralogic compositional information.
- Phyllosilicate spectra in ALH 83100 show Fe-Mg variations around a chondrule rim.
- Effects of crystallographic orientation on the nano-FTIR spectra are shown.

Abstract

Mid-infrared (MIR) spectroscopy has been used with great success to quantitatively determine the mineralogy of geologic samples. It has been employed in a variety of contexts from determining bulk composition of powdered samples to spectroscopic imaging of rock thin sections via micro-FTIR. Recent advances allow for IR measurements at the nanoscale. Near field nanoscale infrared imaging and spectroscopy with a broadband source (nano-FTIR) enable understanding of the spatial relationships between compositionally distinct materials within a sample. This will be of particular use when analyzing returned samples from Bennu and Ryugu, which are thought to be compositionally like CI or CM2 carbonaceous chondrites. Returned samples will likely contain olivine/pyroxene chondrules that have been transformed into hydrous phyllosilicates, sulfides, carbonates, and other alteration phases. The use of near-field infrared techniques to probe the boundaries between once pristine chondrules and alteration phases at the nanoscale is a novel approach to furthering our understanding of the compositional evolution of carbonaceous asteroids and the processes that drive their evolution. Here we report the results of nano-FTIR spectroscopy and imaging measurements performed on the carbonaceous chondrite Allan Hills (ALH) 83100 (CM1/2). We show with nanoscale resolution that spatially resolved Fe-Mg variations exist within the phylosilicates around a chondrule rim. We also present effects of crystal orientation on the nano-FTIR spectra to account for the spectral differences between the meteorite and mineral spectra.

Plain Language Summary

NASA's OSIRIS-REx mission will return a sample of near-Earth asteroid Bennu to Earth in September, 2023. Based on remote sensing analyses of the asteroid, it is expected that the sample will be similar to CI or CM chondrite meteorites. Key remote sensing analyses of Bennu included thermal infrared emission spectroscopy. In this work, we conduct infrared spectral analyses of Allan Hills 83100, a CM 1/2 chondrite that shares spectral similarities to Bennu. We use synchrotron near-field infrared (nano-IR) measurements to analyze the sample at scales of about 30 nm/pixel. This allows us to capture the spectra of very fine-grained components in meteorites that contribute to their overall bulk spectra measured from remote sensing platforms. We document the chemical alteration of a chondrule and show strong alteration gradients in the sample over length scales smaller than 10 microns.

1 Introduction

Mid-infrared (MIR) spectroscopy has been used to great success towards quantitatively determining the mineralogy of geologic samples (Hunt and Salisbury, 1970; Hapke, 1981; Johnson, 1983; Clark and Roush, 1984; King and Ridley, 1987; Mustard and Pieters, 1987). It has been employed in a variety of contexts from determining bulk composition of powdered samples (Lane et al., 2011; Friedlander et al., 2015; Shirley and Glotch, 2019) to spectroscopic imaging of

rock sections via micro-Fourier transform infrared (micro-FTIR) (Yesiltas and Kebukawa, 2016; Jaret et al., 2015, 2018; Farrand et al., 2016, 2018; Yesiltas et al. 2019; Johnson et al., 2020).

The spatial resolution of MIR spectroscopic measurements has typically been limited by the diffraction limit of light, resulting in minimum spot sizes of ~1 μm at synchrotron facilities with bright infrared light sources (Nasse et al. 2011; Yesiltas et al. 2017). In their seminal paper, Amarie et al. (2009) demonstrated the first continuous infrared spectroscopic measurements at nanoscale (~20 nm) resolution, achieved by coupling an FTIR spectrometer with a scanning near field optical microscope (SNOM), the latter of which had already demonstrated nm resolution in the visible wavelength range (Dürig et al., 1986).

The advent of near-field infrared (nano-FTIR) spectroscopy and imaging has allowed for measurement of the vibrational spectra of material monolayers and even single molecule complexes (Xu et al., 2012; Amenabar et al., 2013). The ability to make high signal-to-noise ratio (SNR) measurements at high spatial resolutions makes the nano-FTIR technique an excellent method of analysis when sample availability is low or scientific questions to be addressed require high spatial resolution. This makes nano-FTIR an extremely effective tool for the study of extraterrestrial planetary materials. Dominguez et al. (2014) used nano-FTIR to study the chemistry of a single cometary dust grain from Comet 81P/Wild 2, collected during NASA's Stardust mission. Others have used nano-FTIR to study understand nano-scale mineral and organic compositional variation in carbonaceous and ordinary chondrites, resulting from various parent body alteration processes (Kebukawa et al., 2019; Glotch et al., 2019; Yesiltas et al., 2020, 2021).

The nano-FTIR method, and the previous works that have employed its use, will be of particular use when analyzing returned samples of the near-Earth asteroids Bennu and Ryugu from the OSIRIS-REx and Hayabusa-2 missions respectively. Both of these C-type asteroids are thought

to be compositionally analogous to the CI or CM2 carbonaceous chondrites (King et al., 2015; Kitazato et al., 2019), which have undergone varying degrees of aqueous alteration. Recent results have confirmed hydrated and volatile-rich bulk composition of Bennu as well as the linkage between Bennu and carbonaceous chondrites (Lauretta et al., 2019). Returned samples will likely contain organics, phyllosilicates, carbonates, and other alteration phases (Hamilton et al., 2019, 2021; Kaplan et al., 2020; Breitenfeld et al., 2021). The use of near-field infrared techniques to probe the boundaries between once pristine chondrules and alteration phases at the nanoscale is a novel approach to further improving our understanding of the compositional evolution of carbonaceous asteroids and the processes that drive their evolution.

Furthermore, the use of nano-FTIR imaging and spectroscopy is an excellent tool for understanding organic molecules found within carbonaceous chondrites and asteroid samples, including the identity of those compounds and the spatial relationships between organic compounds and mineralogical phases (Takir et al., 2013; Yesiltas et al., 2013, 2021). This information may prove critical to understanding how complex organic compounds found in meteorites and asteroid samples formed (Pearson et al., 2002; Simon et al., 2020). To that end, here, we report the results of nano-FTIR spectroscopy and imaging measurements performed on the carbonaceous chondrite ALH 83100 (CM1/2), a potential compositional analog for the asteroid Bennu.

2 Materials and Methods

2.1 Petrographic Imaging

A reflected light mosaic of the ALH 83100 thin-section sample was formed by ‘stitching’ together individual microscopy images using the software PtGUI. Individual images used to create

mosaics were captured using a Fein Optic microscope with a 4x objective lens and an AM-Scope MU1403 camera attachment.

2.2. Micro-FTIR Hyperspectral Imaging

We collected a hyperspectral micro-FTIR reflectance map of ALH 83100 using a Nicolet iN10MX imaging spectrometer in the Center for Planetary Exploration at Stony Brook University. The instrument is equipped with a 16-pixel MCT linear array detector operating in pushbroom mode to acquire hyperspectral images over the ~4000–500 cm^{-1} (2.5–20 μm) range. The micro-FTIR image has a spatial resolution of 25 μm per pixel and a spectral resolution of 4 cm^{-1}. We measured a sample-free region of a gold standard for calibration of the collected micro-FTIR data. To display compositional variation across the sample, we utilized spectral indices (wavenumbers, spectral channels, and band depths) to map the band strengths of the 3 μm OH/H_2O feature, the ~2.7 μm OH feature, and the ~7 μm CO_3 feature. The most widely used and simplest method to parameterize the presence and strength of spectral bands is a band depth index (e.g., Clark and Roush, 1984; Viviano-Beck et al., 2014). The band strength (B) is calculated as the ratio of the peak center maximum, C, at frequency ν_C, to C*, the phase value on the continuum between points L and H, located at frequencies ν_L and ν_H, respectively. Mathematically, $\boldsymbol{B = 1 - \frac{C^*}{C} = \frac{aL+bH}{C}}$ where $\boldsymbol{a = 1 - b}$ and $\boldsymbol{b = \frac{\nu_C - \nu_L}{\nu_H - \nu_L}}$. In practice, to increase index consistency in a spectrum that may contain noise, the values of C, C*, L, H, ν_L, ν_C, and ν_H may be averages of 2 or more spectral channels.

2.3 Nano-FTIR Spectroscopy

We acquired nano-FTIR measurements at the Synchrotron Infrared Nano Spectroscopy

(SINS) beamline at the Advanced Light Source (ALS) at Lawrence Berkeley National Laboratory (LBNL) (Bechtel et al. 2020). We collected both near-field infrared images at discrete wavelengths and point spectra of a polished thin-section (~30 μm thickness) of the CM2 chondrite Allan Hills (ALH) 83100. Spectra were collected using a neaspec neaSNOM near field system coupled with a conductive atomic force microscope (AFM) tip for focusing the synchrotron infrared beam source (Amarie et al., 2009; Bechtel et al. 2020). Scattering-type near-field phase and amplitude spectra referenced to a gold standard were collected at harmonics of the AFM tapping frequency. Far-field contributions to the acquired signal are removed by demodulating the signal at higher harmonics of the tapping frequency ($n \geq 2$) (Hillebrand & Keilmann, 2000; Labardi et al. 2000). Second harmonic ($n = 2$) data are presented here as a good compromise between near-field signal and background suppression. Demodulation of the initial signal produces both an amplitude and a phase spectrum. These spectra are to first order analogous with the reflectance and absorbance spectra of typical far-field FTIR measurement (Bechtel et al., 2020), respectively. As such, we will make frequent comparisons between amplitude-reflectance and phase-absorbance in this work. It should be noted that the strong electromagnetic interaction between the AFM tip and the sample surface can distort the shapes and positions of the major vibrational features, sometimes making direct comparisons difficult. The spatial resolution of point spectroscopy measurements is controlled by the radius of curvature of the AFM tip, which is <20 nm. Collected spectra had ~8 cm^{-1} spectral sampling.

For imaging, we used the same neaspec instrument operating in pseudo-heterodyne imaging mode with two tunable lasers centered ~1666 cm^{-1} and ~1000 cm^{-1} respectively. As water has an absorption at ~1600 cm^{-1} (H-O-H bending), we used the 1666 cm^{-1} laser to examine the spatial distributions of hydrated mineral phases within the sample. Measurements made with the

1666-cm^{-1} laser were at the discrete 1675, 1623, and 1572 cm^{-1} wavenumbers, while measurements made with the 1000-cm^{-1} laser were taken at the 1081, 1039, 983, and 944 cm^{-1} wavenumbers. We chose the 10-μm laser to understand spectral variations regarding the prominent 10 μm feature found in silicate minerals. Scanned image area dimensions were 11 μm × 11 μm, and collected images had dimensions of 550 pixels × 550 pixels, yielding an image resolution of 20 nm/pixel. The integration time was 7 ms at each spot, yielding a collection time of ~35 minutes per image. Like the point spectra, phase and amplitude spectral maps were collected at the tapping frequency of the AFM tip.

2.4 Sample and Sampling Location

ALH 83100 is a type 1/2 CM Antarctic meteorite find with a weathering grade of Be, meaning that the presence of moderate rusting and evaporate minerals caused by terrestrial weathering are observed on this sample. It is slightly more hydrated than conventional CM2 chondrites (Zolensky et al. 1997), hence the classification of CM1/2. ALH 83100 is composed of ~85 % hydrous phyllosilicates and contains minor abundances (< 3 wt. %) of magnetite, sulfates, and calcite respectively (Howard et al., 2011; Hanna et al., 2019). It has been extensively altered by aqueous activity (De Leuw et al., 2009). 1.9 wt.% C was identified in ALH 83100 by Alexander et al. (2013). It is composed of ~ 0.76 wt. % insoluble organic material (IOM), in which several amino acids have been detected (Alexander et al., 2007; Elsila et al., 2012). Another 8-9 wt. % of ALH 83100 is made up of the primary ferromagnesian silicate phases olivine and pyroxene in the form of chondrule grains and chondrule fragments. Its carbonate abundance is ~2.8 vol% (De Leuw et al. 2010). For this work, a polished thin section (~30 μm thickness) of ALH 83100 was loaned from the US Antarctic Meteorite collection at Johnson Space Center (JSC). In this sample, we chose to target the interface between one such chondrule and the surrounding fine-grained

matrix. This boundary zone was targeted because it might provide information regarding the aqueous alteration of the primary chondrule minerals into the hydrous phyllosilicate alteration products in the surrounding matrix.

The reflected light microscopy and micro-FTIR composite images of ALH 83100 are shown in Figure 1. The colors shown in the RGB image are representative of common features observed in the spectra of the hyperspectral map image: red represents a relatively strong C-H stretch absorption, green represents a CO_3 (carbonate) stretch reflectance feature, and blue represents a strong O-H stretch absorption feature. Spectra containing O-H stretch features likely represent serpentine minerals, which are hydroxylated phyllosilicates that are common in CM chondrites. These indicate aqueous alteration, making blue zones of particular interest. Based on the prominence of hydroxylated mineral signatures, we chose the chondrule indicated by the arrow in Figure 1a. This chondrule displays strong O-H stretch features and is also bordered by material that is both faintly red and blue in the hyperspectral image. This suggests that the outlying matrix

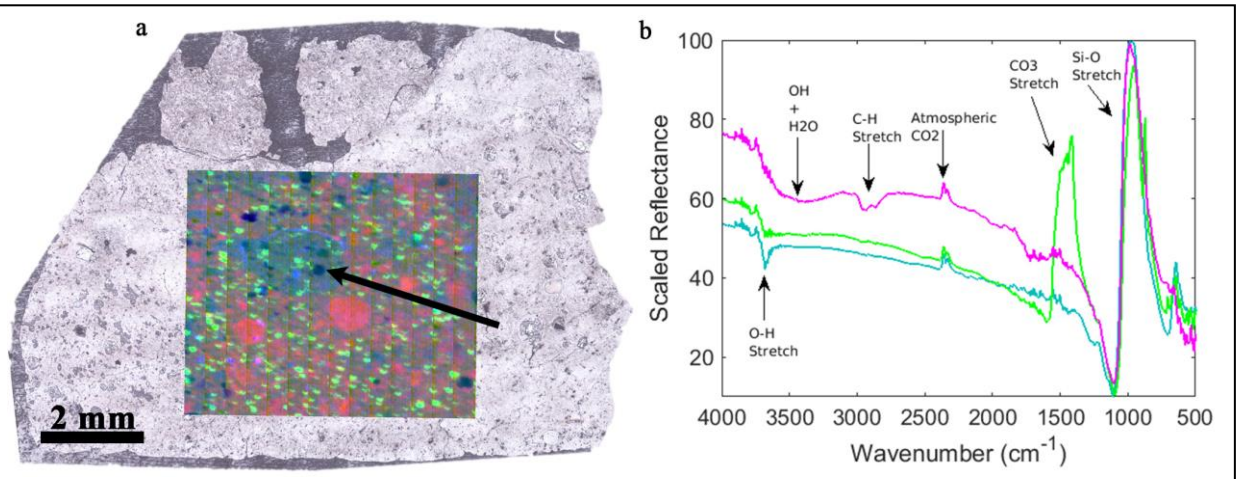

Figure 1. (a) RGB composite micro-FTIR map collected from ALH 83100 overlain on a corresponding reflected light microscopy image mosaic; Black arrow points at the chosen target chondrule shown as a dark blue circle. (b) Scaled micro-FTIR reflectance spectra containing the spectral features to which the RGB pixels of the micro-FTIR hyperspectral map are tied: The pink spectrum contains a strong C-H stretch feature (organic carbon), the green spectrum contains a strong CO_3 stretch feature (carbonate phases), and the blue spectrum contains a strong O-H stretch feature (hydrous minerals).

179 also contains hydrous minerals but also organic carbon. A closer inspection of the chondrule via
180 reflected light microscopy reveals that it is bisected by a large vein (Figure 2). Smaller veins are
181 seen throughout the chondrule. Rather than collect nano-FTIR measurements from these cracked
182 areas, we chose the 'northern' chondrule-matrix interface zone as the measurement area of interest
183 to maximize the compositional variability within the scene. The imaged region includes areas of
184 both chondrule and fine-grained matrix exposure compared to the slivers of matrix in the chondrule
185 interior. Our goal was to capture information regarding the spectral variability of these visibly

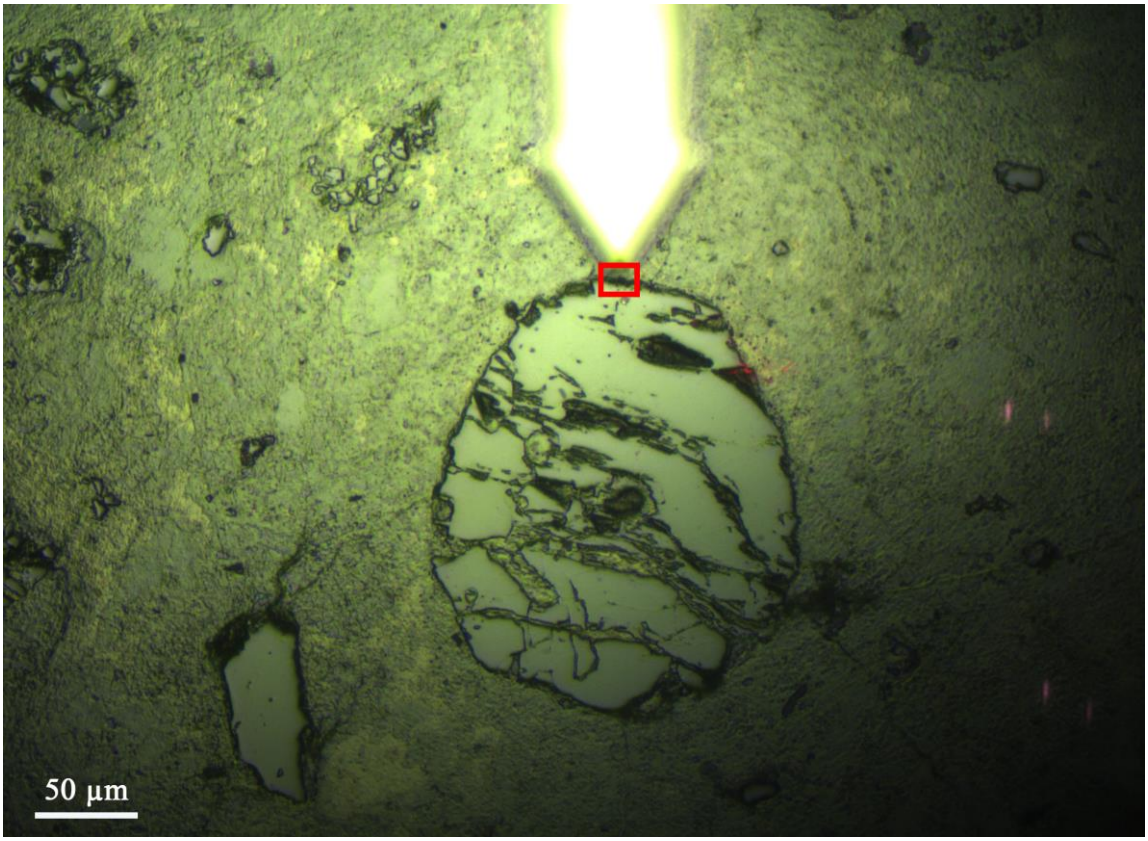

Figure 2. Reflected light microscopy image of the target chondrule; The measurement collection area is the interface between the chondrule and outlying fine-grained matrix, as indicated by the red box at the end of the AFM cantilever.

186 different types of materials as well differences between chondrule and matrix.

187 Nano-FTIR imaging allows simultaneous collection of sample topography with IR images.

The collected topographic map shows a high resolution view of the region of interest (Figure 3a) and clearly delineates the boundary zone of interest between the chondrule and the outlying matrix. The chondrule edge, in the bottom quarter of the map, has relatively high elevation compared to that of the outlying matrix, which makes up the majority of the scan. The low-lying matrix, shown

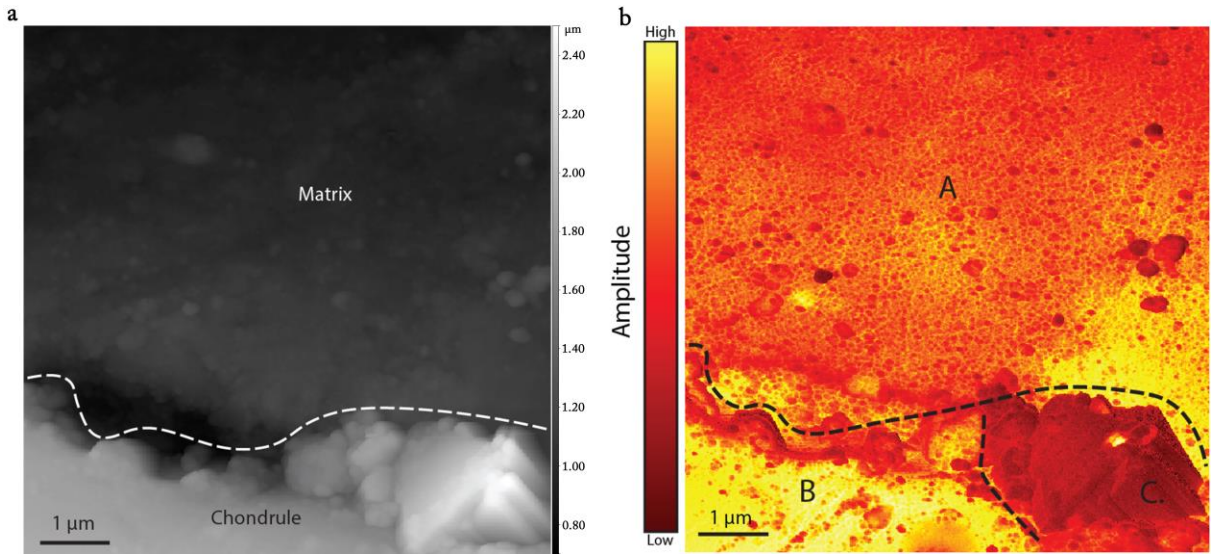

Figure 3. a) Topography map of the chondrule-matrix interface area of interest; White pixels represent locally high topography and black pixels represent locally low topography; Dashed line roughly demonstrates the boundary between the chondrule grain and surrounding matrix; The chondrule grain (bottom-quarter) has relatively high topography compared to the outlying matrix. b) 5.97 μm spectral map of chondrule-matrix interface region of interest; Pixel color represents the amplitude of the 2nd AFM tapping harmonic frequency; Horizontal dashed line shows the chondrule-matrix boundary; Vertical dashed line shows the boundary between the two chondrule zones. Zones A, B, and C represent respectively the outlying matrix, the left portion of the chondrule,and the bottom corner portion of the chondrule.

in shades of dark gray in Figure 3a, contains areas of higher topography. In general, there is some height difference (< 1 μm) between the chondrule grain and the fine-grained matrix area.

4. Results

We collected nano-FTIR images of the selected area of interest at wavelengths of 5.97, 6.16, 6.36, 9.25, 9.621, 10.59, and 10.7 μm. All optical amplitude images shown here are 2nd harmonic optical amplitude images that are normalized within the individual image and are not on

198 a common scale. Beginning with the 5.97 μm map (Figure 3b.), striking compositional variability
199 is observed. The chondrule edge is divided into two section: the bottom left portion, which is
200 largely a high amplitude zone and the area in the right corner of the map, which has the lowest
201 amplitudes of the map. The 5.97 μm optical amplitude of the matrix also varies spatially. High
202 amplitude zones border the chondrule grain, while the top of the map is characterized by broadly
203 low amplitude zones. The area between these relatively homogenous regions of matrix is
204 characterized by the optical amplitude that varies at a spatial scale of < 0.1 μm. Features with radii
205 < 0.5 μm are frequent in this region; these grains are generally low optical amplitude, but still vary.
206 Intra-chondrule variation exists at 6.16 and 6.36 μm as well (Figure 4.). The relationship between
207 the distinct zones of the exposed chondrule edge are maintained at these wavelengths: the left
208 portion has relatively higher optical amplitudes and the right portion has the lowest optical
209 amplitude pixels of the map. At both 6.16 and 6.36 μm, the left portion of the chondrule appears
210 less homogenous than at 5.97 μm. The left portion of the chondrule edge has relatively lower
211 optical amplitude at these wavelengths than at 5.97 μm. The edge of the chondrule at is better
212 defined at these wavelengths as well; the border is much lower optical amplitude than the
213 surrounding matrix at 6.16 and 6.36 than at 5.97. At 6.16 and 6.36 μm, the mottled or web like
214 amplitude variation seen in the matrix at 5.97 μm is even more prevalent. The spectral contrast
215 between the outlying grains and the fine-grained matrix, in which they are suspended, is also more
216 pronounced.

217 At 9.25 and 9.621 μm, intra-chondrule optical amplitude variation still exists (Figure 4.).

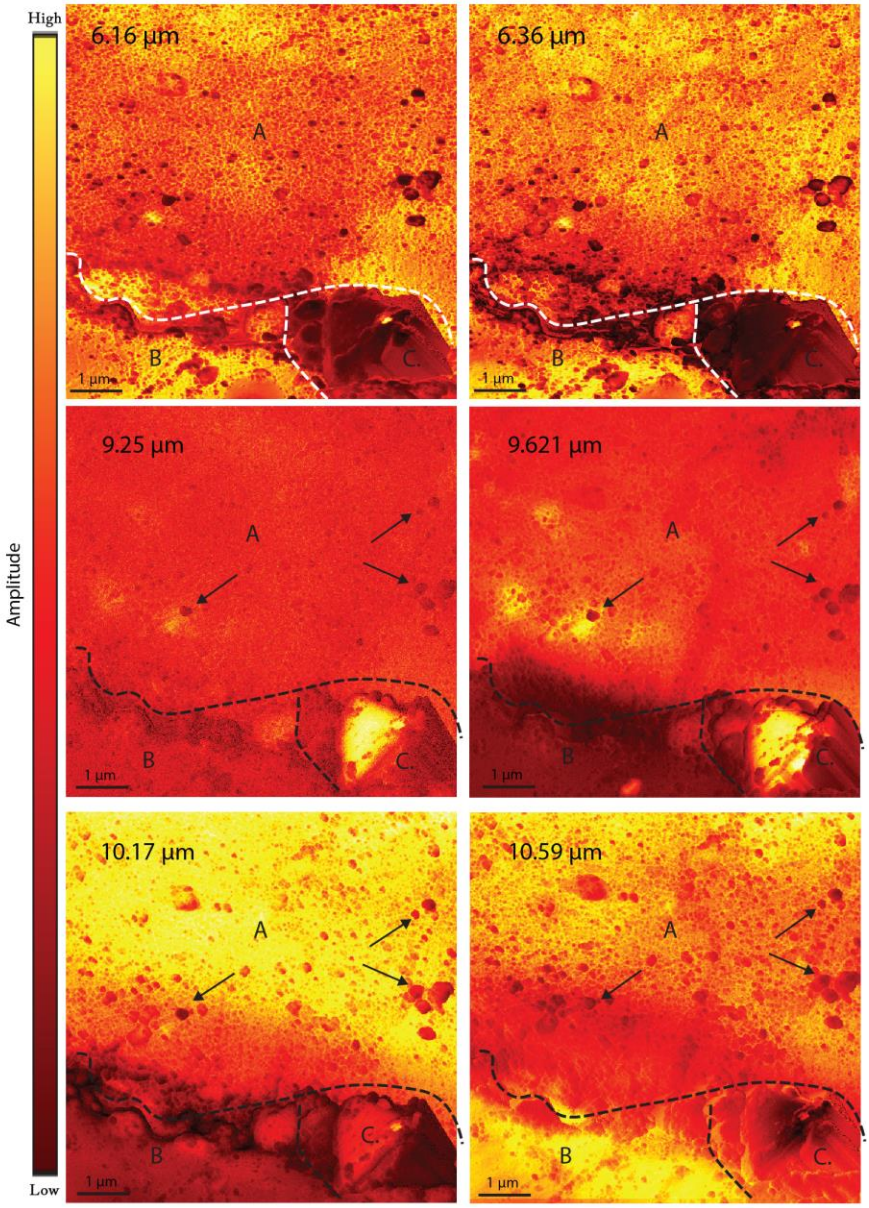

Figure 4. (top row) 6.16 and 6.36 μm spectral maps of chondrule-matrix interface region of interest; (middle row) 9.25 and 9.621 μm spectral maps of chondrule-matrix interface region of interest; (bottom row) 10.17 and 1051 μm spectral maps; Horizontal dashed line shows the boundary chondrule-matrix boundary; Vertical dashed line shows the boundary between the two chondrule zones. Zones A, B, and C represent respectively the outlying matrix, the left portion of the chondrule,and the bottom corner portion of the chondrule. Pixel color represents the relative optical amplitude of the 2nd AFM tapping harmonic frequency; Black arrows indicate 'grains' suspended in the matrix with low optical amplitude values.

218 The left portion of the chondrule exposure is homogenously low optical amplitude at both

wavelengths. In contrast, a part of the bottom right portion of the chondrule is very high optical amplitude at both wavelengths. At 9.25 μm, the outlying fine-grained matrix is largely homogenous with a low optical amplitude but does still exhibit weak nano-scale mottled variation. Suspended grains (black arrows) also have low optical amplitude values at this wavelength. At 9.621 μm, the matrix is less homogenous with enclaves of high optical amplitude material and more extensive nano-scale mottling. The small outlying grains are generally lower optical amplitude than the surrounding matrix at 9.621 μm.

At 10.17 μm, intra-chondrule variation, observed at other wavelengths, has disappeared (Figure 4). Instead, the whole chondrule exposure is characterized by low optical amplitude values. At this wavelength, the fine-grained matrix can be described as two homogenous zones: (1) the middling amplitude border zone (2) the high amplitude outer region. As the name implies, the border portion of observed matrix, which immediately borders the chondrule and extends outward for ~ 1-2 μm radially, has median amplitude values. These values increase as distance from the chondrule grain increases. The outer region of matrix is homogenously high optical amplitude material at this wavelength. Observed variation in this region is caused by the low optical amplitude of the small, suspended grains. At 10.59 μm, intra-chondrule variation returns, with the left portion of the chondrule exposure displaying high optical amplitude values and the bottom right zone having low optical amplitude pixels. There is also widespread variability within the matrix at this wavelength. The matrix border region again has moderate optical amplitude values and is relatively homogenous. Higher optical amplitude pixels and nanoscale amplitude mottling characterize the outer matrix region. The matrix suspended grains all appear to have low optical amplitude values at this wavelength.

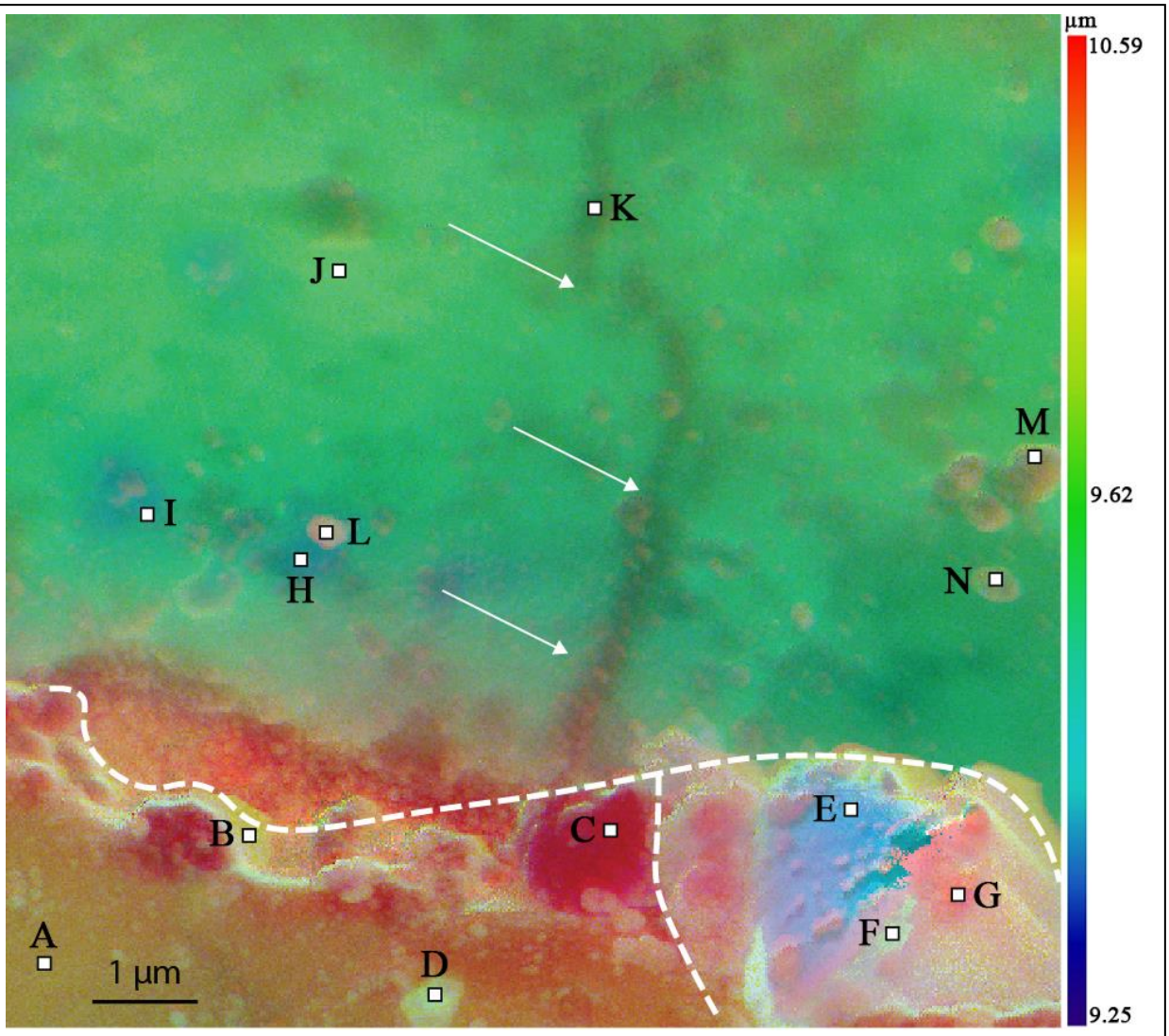

Figure 5. False color RGB image composite of the chondrule-matrix area of interest; R, G, and B color channels represent the 10.59, 9.62, and 9.25 µm wavelengths, respectively. Black edged squares represent positions where single spectra were collected. Arrows point to vein-like structure; Horizontal dashed line shows the chondrule-matrix border; Vertical dashed line shows border between chondrule zones; Points A, B, C, and D lie within the left chondrule zone; Points E, F, and G lie within the bottom right corner chondrule zone; Points H, I, J, K, L, M, and N lie within the matrix zone.

Using the map data collected at three discrete wavelengths, we generated a decorrelation stretched (DCS; Gillespie et al., 1986) false-color image that provides a clearer picture regarding the compositional variability in this portion of the sample.The color channels of the DCS map, R, G, and B represent the 10.59, 9.62, and 9.25 µm wavelengths, respectively. The exact data used to create the DCS maps, were individual 2nd harmonic phase maps for each wavelength, meaning that

the color of a pixel is tied to the phase value of its counterpart pixel from each relevant wavelength map. The DCS map (Figure 5) shows which areas of the map are spectrally similar and dissimilar, and corroborates observations of the individual wavelength maps. There is widespread spectral variability within the chondrule grain, within the matrix, and between the chondrule and matrix. The composite map displays the spectral contrast between the left portion of the chondrule exposure and the bottom right zone. In the composite map, the bottom left is shown in yellow and orange while the bottom right is mainly blue. The edge regions of the chondrule have coloring of pinks and red, distinguishing themselves from the more interior portions of the grain. The fine-grained matrix shown in Figure 5 is green, suggesting a maximum optical amplitude around 9.62 μm, with minor variations in color and brightness. The observed small grains suspended in the fine-grained matrix vary in color, between orange, pink and blue, suggesting substantial spectral variability. Interestingly, this map also reveals a long vein like structure (white arrows), which had been obscured in the individual optical amplitude maps. This structure extends out radially from the chondrule exposure for ~8 μm and has a width of 0.25-0.33 μm.

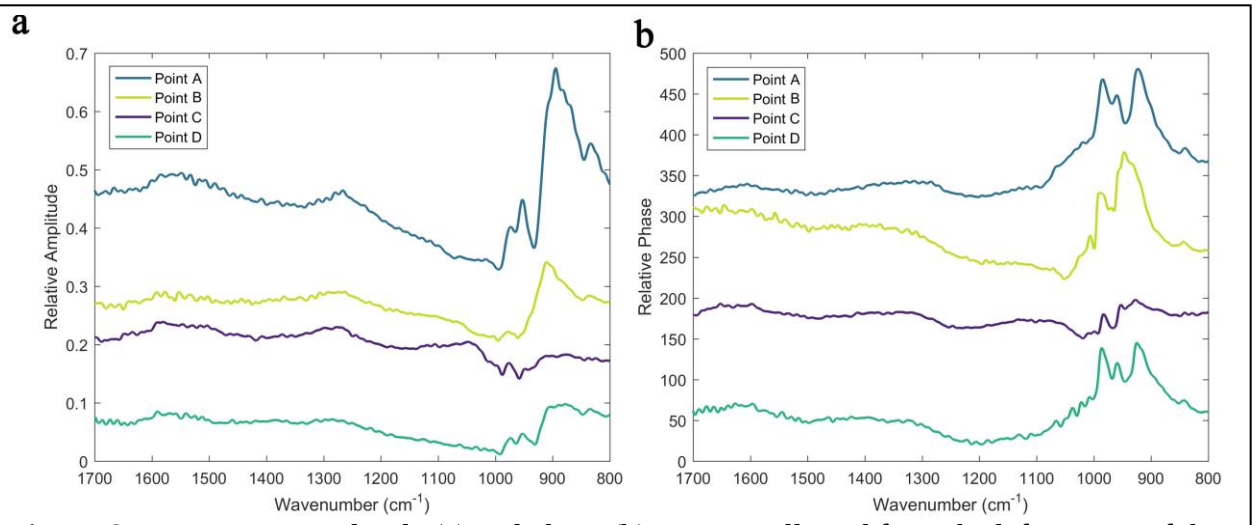

Figure 6. Nano-FTIR amplitude (a) and phase (b) spectra collected from the left portion of the chondrule exposure; Spectra have been stacked for comparison; amplitudes and phases are relative.

On the basis of spectral variability observed in the individual optical amplitude images and the false color DCS map, we collected point spectra from various positions within the area of interest. The positions from which the point spectra were collected can be seen in Figure 5. These point spectra were collected from areas that belong to four categories: the left portion of the chondrule exposure, the bottom right corner zone of the chondrule, the fine-grained matrix, and the grains suspended in the matrix.

We collected spectra from four positions, A, B, C, and D, within the left portion of the chondrule exposure (Figure 6). Amplitude spectrum C is relatively flat but has noticeable a broad maximum centered at 1050 cm^{-1}. Spectrum A, by contrast, has a prominent amplitude maximum at 890 cm^{-1} and several smaller features at 830, 950, and 970 cm^{-1}. Spectrum D also has a broad amplitude maximum centered around 890 cm^{-1}, with additional features at 950 and 970 cm^{-1}.

Phase spectra show that A and D have similar spectral profiles. They both have a triplet with bands at 920, 960, 985 cm^{-1}. Spectrum B has a different profile. It presents prominent bands at 950 and 990 cm^{-1} and a smaller feature at 1000 cm^{-1}. Similar to the amplitude spectrum, the phase spectrum of C contains relatively weak features but bands at 927, 953 and 985 cm^{-1} are still visible.

From the bottom corner zone of the chondrule exposure, we collected spectra from three positions: E, F, and G. The amplitude spectrum of point E (Figure 7.) shows one prominent maximum centered at 1030 cm^{-1} and an ancillary feature at 970 cm^{-1}. Spectrum F has amplitude at the same positions as spectrum E, but with lower amplitudes. The amplitude spectrum of point G has less intense features. Their corresponding phase spectra are noiser. Spectrum E has a broad peak with maxima at 1100 cm^{-1} and extends up to 1400 cm^{-1}. Spectra F and G have a maxima at

282 1082 and 1055 cm^{-1} respectively. As in the amplitude spectra, these broad bands have decreasing
283 intensity as well, with spectrum E having the most intense peak.

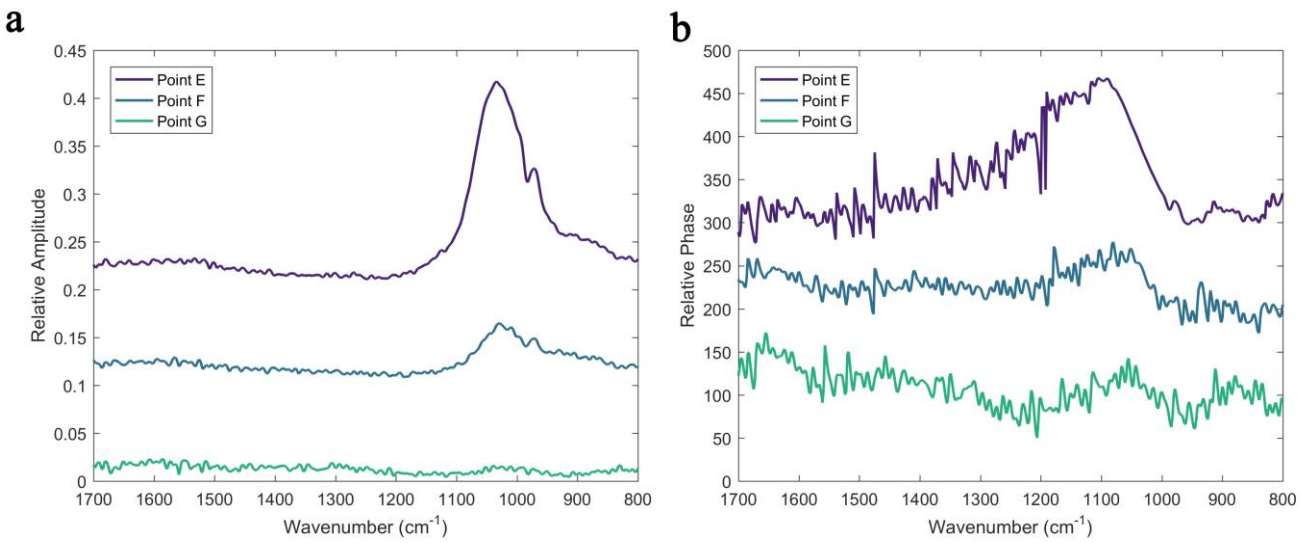

Figure 7. Nano-FTIR amplitude (a) and phase (b) spectra collected from the bottom corner zone of the chondrule exposure; Spectra have been stacked for comparison; amplitudes and phases are relative.

284 We collected additional spectra, shown in Figure 8, from four positions in the outlying
285 fine-grained matrix: H, I, J, and K. The amplitude spectrum of Point H has two amplitude maxima
286 at 970 and 1020 cm^{-1} and a third broad maximum centered at ~850 cm^{-1}. Spectrum K has a single
287 broad maximum centered around 960 cm^{-1}, and spectrum J has the same feature with an overall
288 higher amplitude. Spectrum I has a prominent amplitude maximum at 1030 cm^{-1} and a smaller
289 feature at 970 cm^{-1}.The phase spectra of these points present a prominent and well-defined peak

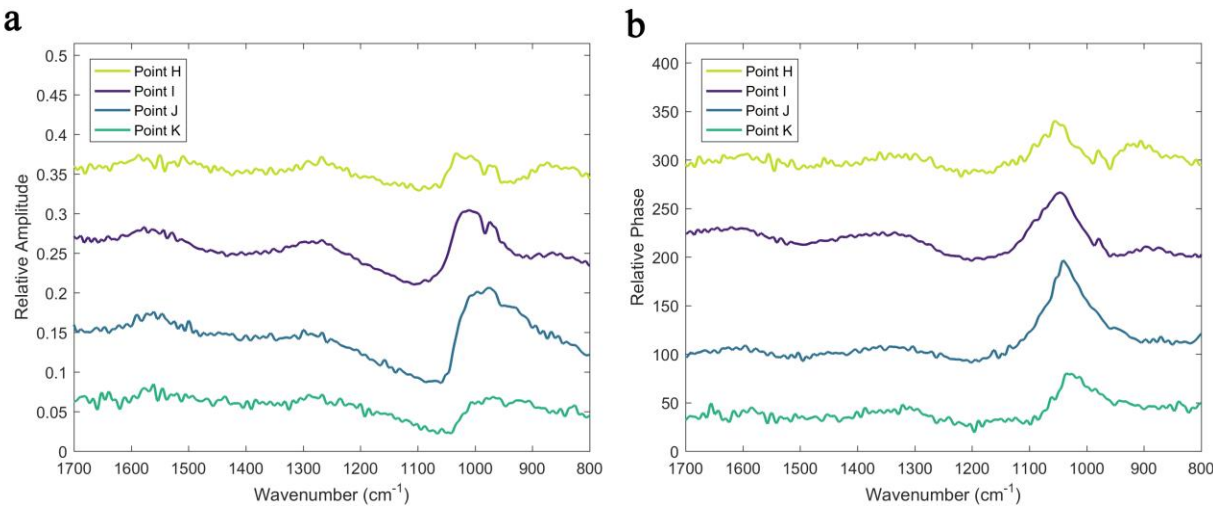

Figure 8. Nano-FTIR amplitude (a) and phase (b) spectra collected from the fine-grained matrix of the region of interest; Spectra have been stacked for comparison; amplitudes and phases are relative.

near 1040 cm^{-1}. Spectra I and H additionally present a weaker band at 980 cm^{-1}, which is not resolved in spectra K and J.

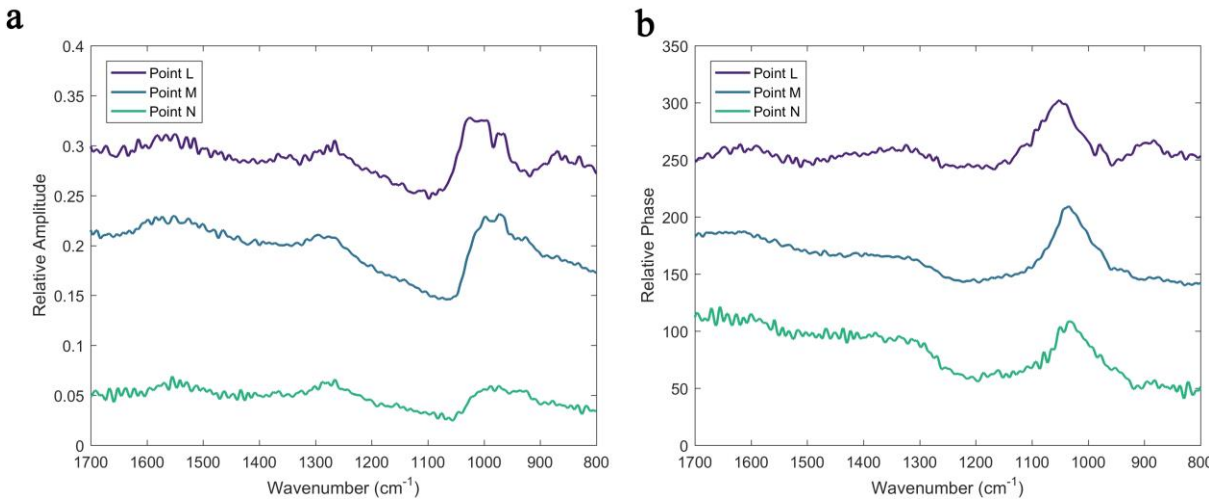

Figure 9. Nano-FTIR amplitude (a) and phase (b) spectra collected from grains suspended in the fine-grained matrix zone of the region of interest; Spectra have been stacked for comparison; amplitudes and phases are relative.

Finally, three spectra were collected from positions on grains suspended in the fine-grained matrix: L, M, and N (Figure 9.). Amplitude spectrum L has amplitude maxima at 970 and 1020 cm^{-1}. Spectrum M also has two maxima at 970 cm^{-1}, the other at 1000 cm^{-1}. Finally, spectrum N

295 is relatively flat, but has a broad maximum centered at 980 cm^{-1}. Their corresponding phase spectra
296 present a broad symmetric band centered around 1030-1050 cm^{-1}. A smaller feature at 978 cm^{-1}
297 and a broad bump at 896 cm^{-1} are also present in spectrum L. We note that most of the spectra
298 presented here also have a broad feature near 1275 cm^{-1}.

299 **5. Discussion**

300 We place the point spectra collection positions, described in the results section, into two
301 main groups. The spectra collected from member positions of a given group share similar feature
302 positions and overall line shapes, in both their amplitude and phase spectra. This suggests that the
303 materials represented by the positions/point spectra of a group are compositionally similar. We
304 also define a third group containing points with flat and featureless spectra. Points E and N belong
305 to this group and are omitted from discussion.

306 The members of group 1 are spectra A, D and B. Spatially, points A and B exist on the
307 inner portion of the chondrule exposure, ~1-1.5 μm from the chondrule-matrix boundary, while
308 point B is on the chondrule rim. The amplitude spectra of these points are dissimilar; spectra A
309 and B have sharp, well-defined reflectance features while spectrum D has weaker and broader
310 features. However, all three spots have spectral features at similar positions. Furthermore, when
311 we observe the phase spectra of each position the relationship becomes much clearer. Figure 10
312 shows a comparison of the amplitude and phase spectra of positions A, D, and B, as well as nano-
313 FTIR amplitude and phase spectra of single crystal enstatite (this study) , forsterite (Dominguez et
314 al., 2014), and olivine chondrule spectra from Yesiltas et al. (2020). The phase spectra of points A
315 and D have prominent features around 925, 960, and 985 cm^{1}, suggesting that the material these
316 spectra represent are compositionally similar. The difference in strength of observed features in

the amplitude spectra A and D are likely a result of local crystal orientation (Figure 11). These spectra match closely the nano-FTIR spectra of olivine in Didim (H3-5 chondrite) (Yesiltas et al. 2020). The forsterite nano-FTIR amplitude spectrum of Dominguez et al. (2014) appears different than the amplitude spectra of points A, D, and B.While there are observable shifts in feature positions between the point spectra and the pure forsterite spectrum, the point spectra resemble the forsterite spectrum more closely than that of the pure enstatite spectrum. Furthermore, the amplitude spectra of points A, D, and B are also in disagreement with amplitude spectra (Dominguez et al., 2014) and emissivity spectra of pyroxenes (Hamilton, 2000). Therefore, we

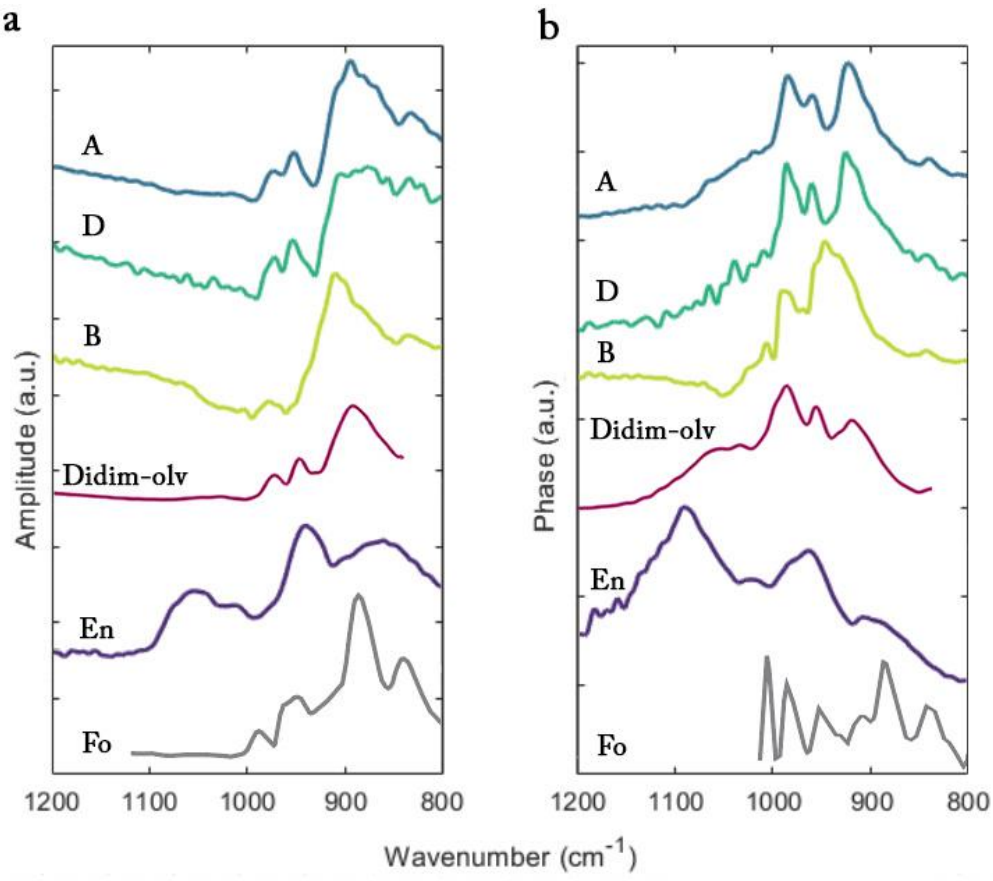

Figure 10. Amplitude (a) and phase (b) spectra of points A, D and B with amplitude spectra of single crystal enstatite (En) and forseterite (Fo); Enstatite spectra are from this study; forsterite spectra taken from Dominguez et al. (2014), Olivine chondrule spectrum is from Yesiltas et al. (2020). Spectra are normalized and offset for comparison.

interpret the spectra of A, D, and B as olivine with spectral differences resulting from variable crystal orientation.

In amplitude spectrum A, we attribute features at 895 cm^{-1}, 952 cm^{-1}, 974 cm^{-1} to the asymmetric Si-O stretch (ν_3) and the 832 cm^{-1} feature to the symmetric O-Si-O stretch (ν_1) (Reynard et al., 1991; Hamilton, 2010). While identifying olivine as the material observed at points A, D, and B is relatively straightforward, understanding exact forsterite-fayalite composition is less so. Chondrules in CM chondrites are observed to have Fe/Mg ratio values < 0.4 (Hezel &

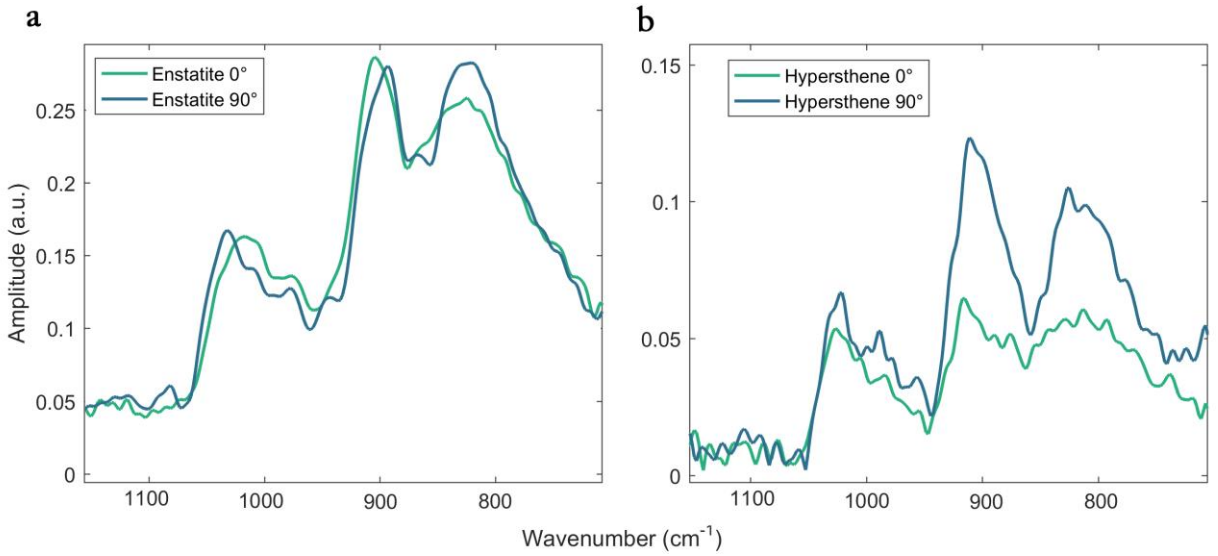

Figure 11. (a) Nano-FTIR amplitude spectra of single-crystal enstatite; These spectra were collected from the same crystallographic face (a-face) but offset by a 90˚rotation. (b) Nano-FTIR amplitude spectra of a single-crystal hypersthene; These spectra were collected from the same crystallographic face (a-face) but offset by a 90˚rotation; Both spectral pairs demonstrate that changing crystal orientation can cause shifts in band position and strength.

Palme, 2010; Palme et al., 2015; Friend et al., 2016), likely resulting from the high resistance of Mg-rich silicates to aqueous alteration (Zolensky et al., 1993). This suggests that the sample olivine is forsteritic in composition. However, chondrule rims and zones 4-15 μm from the rims of chondrules once subjected to aqueous alteration processes have been observed to have significant Mg depletion compared to the chondrule core (Kereszturi et al., 2014; Kereszturi et al.,

2015). A large body of both experimental and modelling work investigating the MIR spectral properties of the forsterite-fayallite olivine solid solution has been conducted (Duke & Stephens, 1964; Burns & Huggins, 1972; Dorschner et al., 1995; Fabian et al., 2001; Dyar et al., 2009; Hamilton, 2010; Lane et al., 2011). Collectively, these works demonstrate that there is a relationship between the peak positions of various MIR spectral bands and the ratio of Mg/Fe cations that fill the olivine M1 and M2 sites.

Lane et al. (2011), produced several, highly correlative ($R^2 \geq 0.9$) linear functions describing the relationship between a spectral band's peak position and the forsterite content of an olivine sample. Applying these functions on the amplitude spectra of points A and D would suggest that the represented material is an Fo_{70} – Fo_{90} olivine. It's clear from this body of literature that the MIR behavior of olivine spectra also depends on the cationic impurity and crystallographic orientation of a sample. Crystallite sizes of olivine may also effect the spectral band positions (Hamilton et al. 2020). Indeed, comparison of the same spectra with Hamilton et al. (2020) indicates relatively less forsteritic composition (Fo_{35} – Fo_{60}). Furthermore, the strong electromagnetic coupling between the sample and the AFM tip distorts the vibrational modes of a sample, resulting in shifts of band positions and changes in band shape. As a result, our interpretation should be treated with caution.

Figure 11 shows two examples of the dependance of nano-FTIR spectra on crystallographic orientation. This figure displays four spectra; two collected from a single enstatite crystal and two collected from a single hypersthene crystal. In both cases the crystal was oriented, so the IR source was normal to the crystallographic a-face but separated by a 90˚rotation with respect to the normal vector of the a-face. For both minerals, rotation by 90˚ leads to shifts in band position of the mineral's MIR features. Changing the orientation of the crystal can also diminish the strength of a

given feature. The difference in strength of features in the two hypersthene spectra is similar to the difference observed between the features of amplitude spectra A, D, and B. The crystal orientation along with cation impurity and material form further obfuscate the role of Mg/Fe in the positions of olivine nano-FTIR spectra. Further investigation into the relative importance of these variables is required.

The other major position group, Group 2, has the most members: points L, H, K, J, E, I, M, F, and N. Most of the points are in the fine-grain matrix or the suspended grains therein, but points E and F are located in the bottom right corner zone of the chondrule exposure. While band feature strength and exact position vary, each spectrum has a prominent amplitude maximum between ~990-1010 cm^{-1} and an ancillary feature ~940-970 cm^{-1} (Figure 12a). The vertical red line at 1000 cm^{-1} clearly shows the spectral shift of the main silicate band from 990 to 1010 cm^{-1}. The phase spectra are largely in agreement as well, with each spectrum having one main prominent feature between 1040 – 1100 cm^{-1}. A small feature at ~970 cm^{-1} is also observed in some spectra. Based on the general position of the main absorption feature in the observed phase spectra, the materials that these points represent are likely hydrous phyllosilicate minerals. The main phyllosilicate band, which is caused by Si – O stretching vibrations in the SiO_4 molecules composing the mineral's tetrahedral sheet, occurs ~1000-1100 cm^{-1} (Brindley & Zussman, 1959). This is a reasonable assignment, as ALH 83100 has been observed to be composed of ~ 85 % hydrous phyllosilicates (Howard et al., 2011) and the observed amplitude spectra are consistent with reflectance spectra of previous measurements of ALH 83100 (Lindgren et al., 2020). Furthermore, we have shown the area surrounding the observed chondrule is rich in OH bearing material (Figure 1). The exact

phyllosilicate observed in each spectrum is debatable, however we limit possible phases to those readily observed in CM2 chondrites.

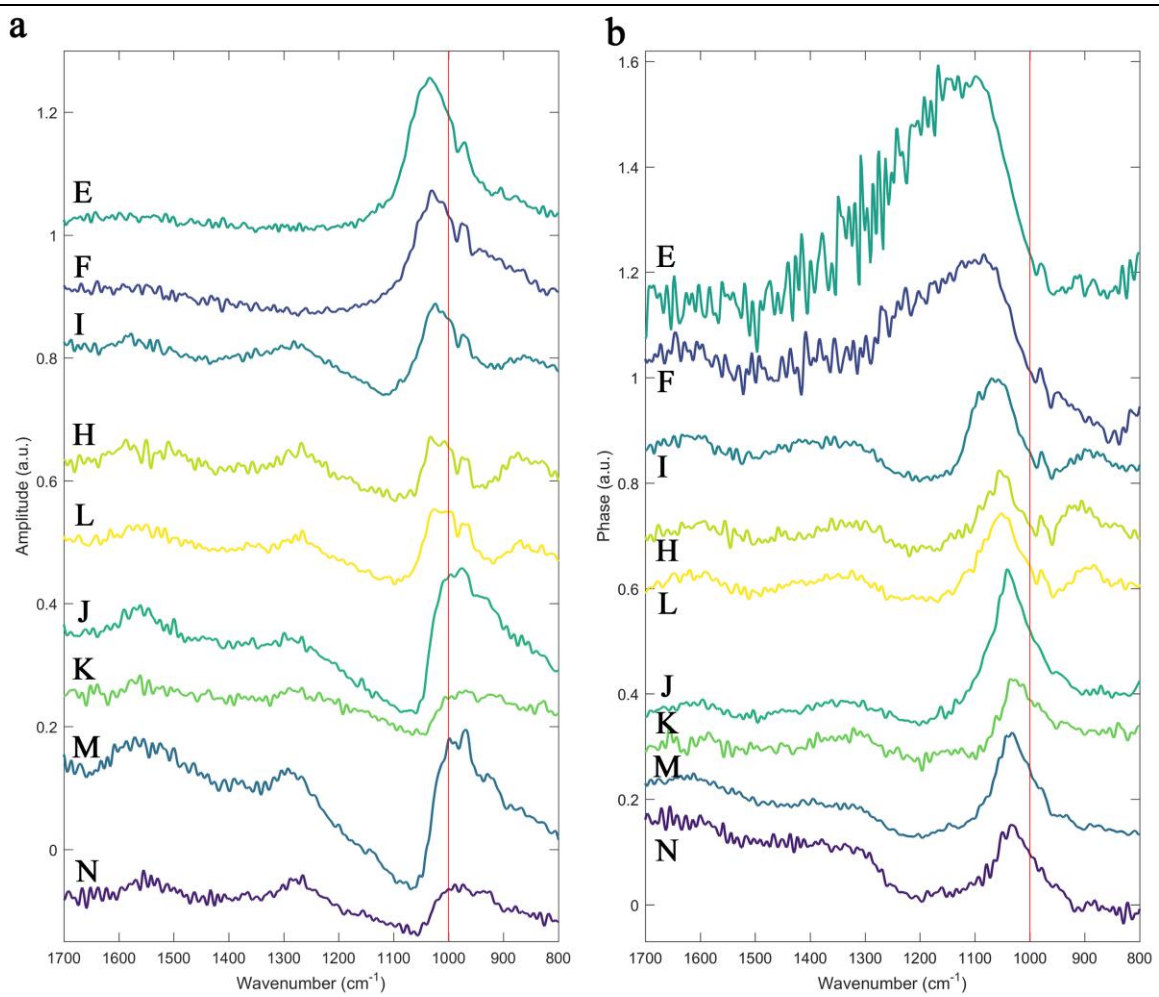

Figure 12. Amplitude (a) and phase (b) spectra of points E, F, H, I, J, K, L, M, and N; Spectra are normalized and arranged by the position of the major feature, from lowest to highest wavenumber for comparison.

The Mg-rich serpentines (chrysotile, antigorite, lizardite) and Fe-cronstedtite are observed in both matrix and the rims of chondrules in CM2 chondrites (Zega & Buseck, 2003; Velbel & Palmer, 2011) and make up ~62 and ~20-24 vol % of ALH 83100 respectively (Howard et al., 2011; Lindgren et al., 2020). MIR spectra of cronstedtite and cronstedtite-rich mixtures are largely in disagreement with the spectra of points E, I, and F shown in Figure 12. (Bates et al., 2020; Breitenfeld et al., 2020). Using laboratory emissivity spectra and Kirchhoff's law (R=1-E), we

389 show that the amplitude spectra of points E, I, and F are in good agreement with the reflectance
390 spectrum of antigorite (Breitenfeld et al., 2020) (Figure 13). In contrast, the amplitude spectra of
391 points K, J, M and N are in poor agreement with the reflectance spectra of saponite and antigorite.
392 However, amplitude spectra K, J, and N match up quite well with the reflectance spectrum of

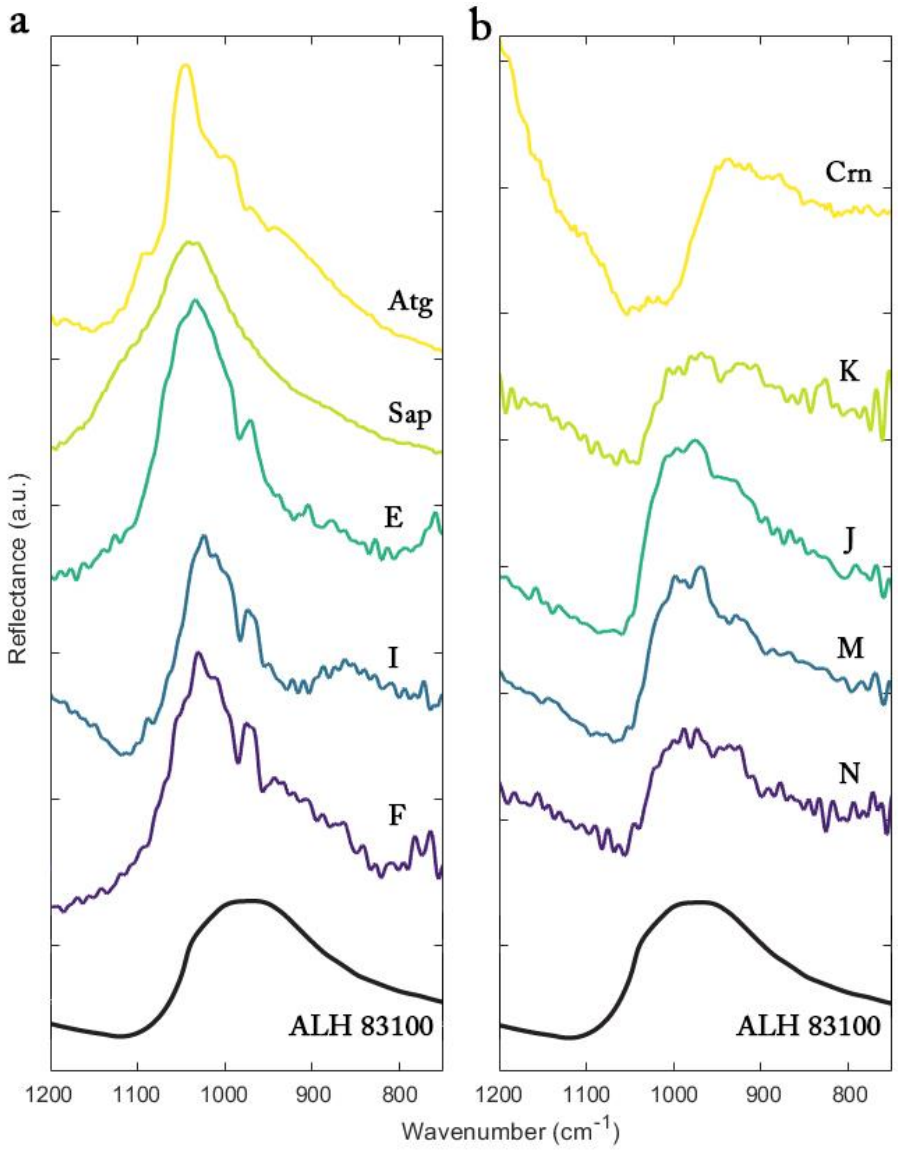

Figure 13. (a) Reflectance spectrum of pure antigorite and saponite pellets (Breitenfeld et al., 2020) and the amplitude spectra of points E, I, and F. (b) Reflectance spectrum of pure cronstedtite (Breitenfeld et al., 2021) and amplitude spectra of points K, J, M, and N; Spectrum ALH 83100 reproduced from (Lindgren et al., 2020). Spectra are normalized and offset for comparison.

393 cronstedtite (Figure 13). Finally, reflectance spectra L and H do not have exact agreement with

either pure mineral phase. Rather, theses spectra appear to be intermediates of the Fe and Mg rich phyllosilicate phases.

The existence of multiple phyllosilicate phases is also supported by the observed variation in band position and overall shape of these spectra. Phase spectra K, J, M, and N have Si-O bend positions around 1029, 1039, 1034, and 1034 cm^{-1} respectively. In terms of amplitude, spectra K, J, M, and N each have a prominent maximum centered around 968, 987, 986, and 984 cm^{-1}. Phase spectra L, H, and I have their Si-O bend positions shifted to higher wavenumber (lower wavelength) with positions ~ 1050.91, 1052.22, and 1064.87 cm^{-1}. These three spectra also are observed to have an additional absorption feature at ~900 cm^{-1}. Amplitude spectra L, H, and I also have prominent reflectance features at 1009, 1016, and 1019 cm^{-1}, respectively. Finally, phase spectra E and F have an Si-O bend feature shifted to even higher wavenumbers at ~ 1086 and 1102 cm^{-1}. The broad shape (full-width ~300 cm^{-1}) of this feature in phase spectra E and F contrasts with the relatively thin/sharp features observed in the other phase spectra of this group.

The spectral differences observed within this group of spectra are spatially distributed, agreeing well with zones of optical amplitude variation observed in the 10.17 μm map displayed in Figure 4. The position of the Si-O bend feature, in both amplitude and phase spectra, shifts to shorter wavenumber as distance from the chondrule rim grows. The respective Si-O features of spectra E and F have the highest wavenumber positions and were collected from the chondrule rim. Spectra L, H, and I have intermediate wavenumber positions of their Si-O bending feature and were collected from the zone of intermediate optical amplitude (orange colored matrix) of the 10.17 μm map. Finally, spectra K, J, M, and N have the lowest wavenumber values of their Si-O bending feature and were collected from the broad zone of high optical amplitude in the 10.17 μm map. We plot and compare the band position parameters of both phase and amplitude spectra in

Figure 14, which shows a strong polynomial-like correlation between the Si-O bending feature band positions observed in phase and amplitude spectra for a given point. We include the Si-O bending feature's band position from the reflectance spectrum of pure cronstedtite and antigorite, seen in Figure 15, to show that the spectra appear to exist on a continuum between the two pure mineral phases. We also show the spatial distribution of the points of interest as colored fields in

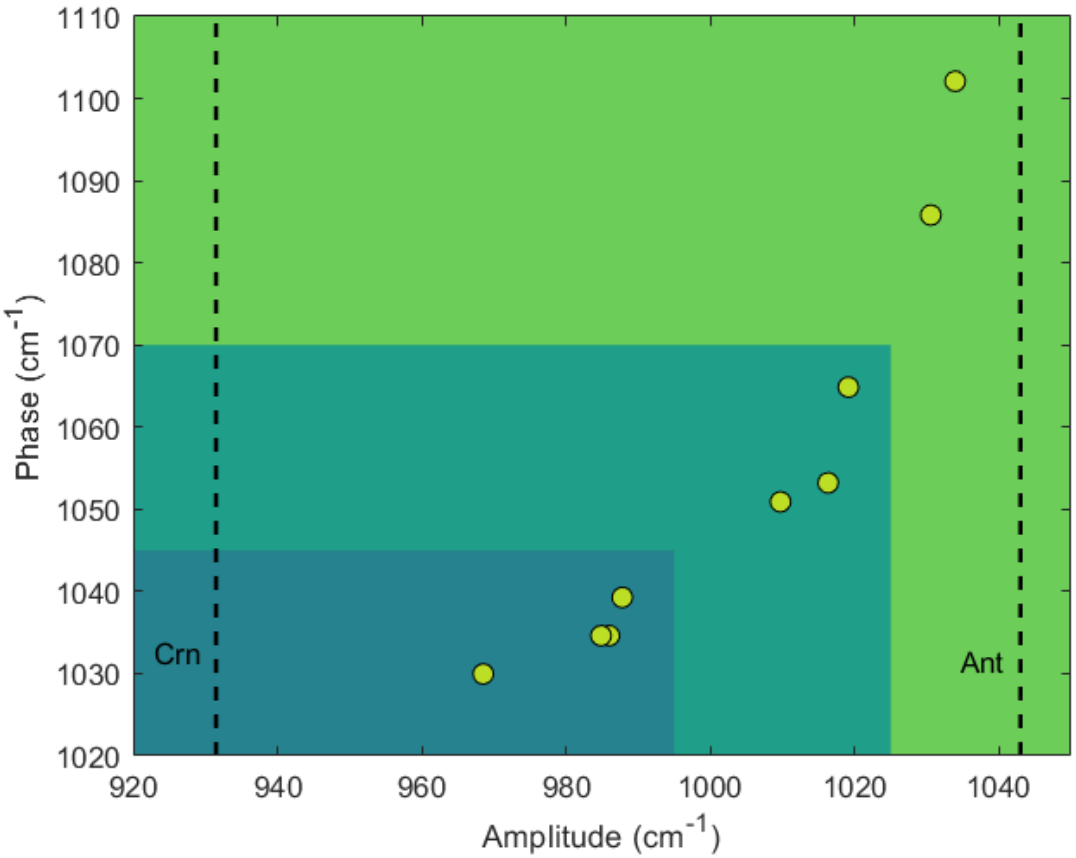

Figure 14. Phase position vs. Amplitude position of the Si – O bending feature observed in the spectra of points L, H, K, J, E, I, M, F, and N. Spectral parameters of these points are represented as yellow markers. Black dashed lines represent the values of the Si – O bend feature band positions observed in the reflectance spectra of pure cronstedtite (Crn) and pure antigorite (Ant). Color zones indicate the spatial distribution of collected spectra in reference to the chondrule rim; Light green (upper-right) zone represents points collected on the rim of the chondrule (E and F); Dark green (middle) zone represent points collected from an intermediate distance from the chondrule (L, H, and I); Blue (bottom-left) zone represents points collected from a relatively large distance (> 2 μm) from chondrule rim. The spatial correlation of compositionally similar materials suggests variable Fe-Mg enrichment/depletion levels with respect to distance from the chondrule rim.

Figure 14. This figure shows that the points with spectra most in agreement with cronstedtite exist furthest from the chondrule rim and spectra most like antigorite exist close to or on the chondrule rim. As such, these data provide evidence for variable Fe-Mg enrichment/depletion zoning around the chondrule rim. Such evidence (Mg-rich/Fe-poor vs. Mg-poor/Fe-rich parts of the rim) suggests that aqueous alteration experienced by ALH 83100 may have occurred in the parent body as well as in the solar nebula as nebular alteration results in the mixing of different phyllosilicate components (Brearley and Geiger, 1991) as observed in some CO3 chondrites (Brearley, 1990, 1991). Additional investigations of chondrule rims in this and other CI/CM meteorites need to be investigated to provide a better constraint on the origin of alteration for the rims.

All discussion thus far has considered spectral features within the wavenumber range of ~800-1200 cm^{-1}. The low wavenumber cutoff is due to the MCT detector used in this work. However, in higher wavenumber amplitude spectra, broad but well-defined features around 1250, 1560, 2300, and 2600 cm^{-1} are observed (Figure 15). For phase spectra, features are seen around 1340, 1600, 1850, and 2375, and 2650 cm^{-1} can be observed in certain spectra. However, it remains

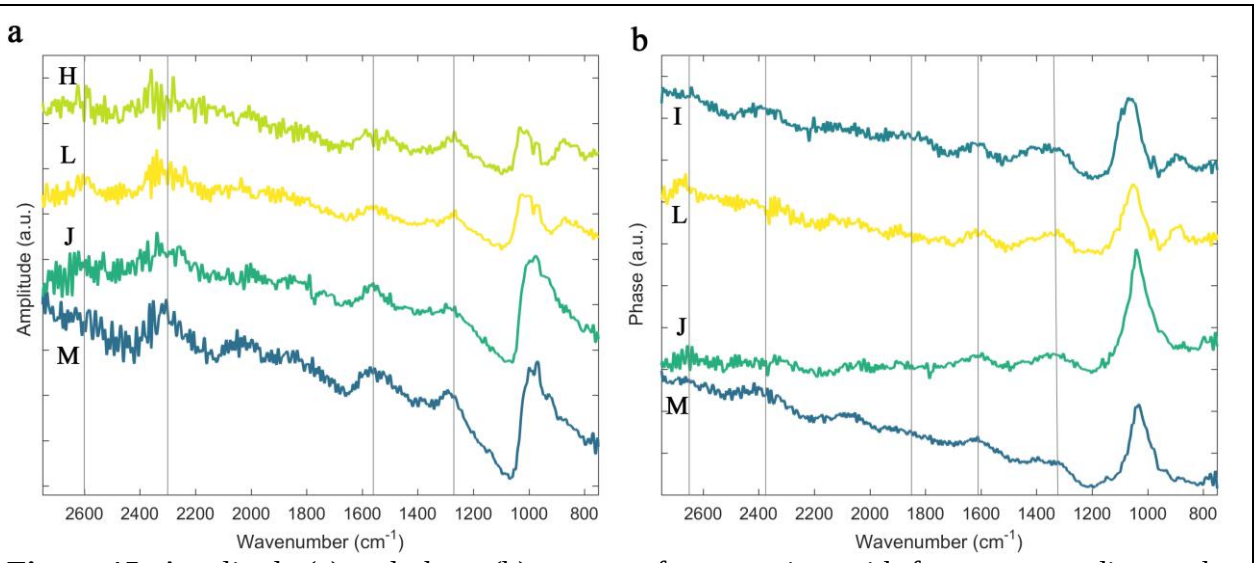

Figure 15. Amplitude (a) and phase (b) spectra of some points with features extending to the higher wavenumbers region. Vertical gray lines indicate positions of bands at higher wavenumbers.

436 unclear whether these features correspond to actual molecular vibrations or are artifacts introduced
437 by the nano-FTIR experimental setup.

438 An argument for these bands being artifacts rather than representing molecular vibrational
439 modes is that they appear consistently in the spectra of mineral phases we've identified as
440 structurally distinct (e.g., olivine vs. antigorite). They appear somewhat repetitive. However, this
441 is not the case for all points; the spectra of points E and F do not have these observed features.
442 Furthermore, the features seen at higher wavenumbers are not characteristic of silicate vibrational
443 modes. Rather the features seen in the 1250-3000 range are more likely the result of carbon bond
444 based absorptions. The C=C vibration (ν), a characteristic feature of insoluble organic matter
445 (IOM), has a corresponding absorption at ~1600 cm^{-1} (Orthous-Daunay et al., 2013). Furthermore,
446 the CH_2 (δ_s) vibration has absorptions at 1300-1400 cm^{-1} (Fuente et al., 2003). As carbonaceous
447 molecules are a large component of carbonaceous chondrites, observed carbon absorption features
448 are not a surprising result.

449 While there is agreement between the high wavenumber features and carbon-based
450 absorptions, there are still issues with definitively assigning vibrational modes to the observed
451 features. These features occur with a periodicity; starting with the 1250 feature in amplitude
452 spectra, they continually occur ~300 cm^{-1} apart consistently. The features appear oscillatory,
453 occurring as broad peaks with broad troughs separating them (Figure 15). Nano-FTIR has a depth
454 sensitivity of 50-100 nm and the observed features could potentially be due to the material within
455 the meteorite sample. This sinusoidal behavior is consistent with that of spectral interference
456 fringes, resulting from internal reflections within thin material films (Teolis et al., 2007; Azarfar
457 et al., 2018). While thin phyllosilicate layers could provide a structure for internal reflections to
458 occur, an alternative material to compose a possible thin film, in this sample, is IOM. The main

459 evidence that internal reflections, due to the thin platy structure, of a phyllosilicate ring are not at
460 play is that interference fringes are seen in the spectra of points representing both olivine and
461 phyllosilicates. These olivine points likely do not have overlying phyllosilicate materials but could
462 have thin overlying IOM films. The 1.9 wt.% C content of ALH 83100 (Alexander et al. 2013)
463 may account for such IOM thin films.

464 In summary, the sinusoidal features observed are likely not actual reflectance or absorption
465 features representing a specific carbon vibration. Rather they are the result of internal reflections
466 of light within IOM materials within the sample. This phenomenon makes identification of specific
467 organic functional groups and therefore specific carbonaceous molecules difficult if not
468 impossible. Ironically, this behavior is also currently the best evidence of carbonaceous molecules
469 in the sampled area of interest (via nano-FTIR).

470 **6 Conclusion**

471 We have presented nano-FTIR images and spectra of the carbonaceous chondrite ALH
472 83100. From the spectra, we have identified olivine, Mg-serpentine and cronstedtite. The focused
473 area includes a chondrule, its rim and the matrix. The spectra representing the chondrule indicates
474 a forsteritic composition (Fo_{70-90}), while the spectra of phyllosilicate minerals within the rim and
475 nearby matrix revealed that there is a spatial distribution of Fe-Mg enrichment/depletion
476 surrounding the chondrule rim. This suggests a heterogeneous aqueous alteration of the rim in the
477 parent body and hence the heterogeneous composition for the rim. Varying Fe-Mg distribution in

the rim might also indicate aqueous alteration for ALH 83100 in the parent body as well as in the solar nebula.

This is the first study to apply multi-spectral IR imaging of a meteorite at the nano-scale. In the context of meteoritics, nano-FTIR spectroscopy and imaging are still novel techniques. Further quantitative analyses of this and other extraterrestrial samples will be enabled by the creation of nano-FTIR mineral spectral libraries that account for crystal orientation and development of methods to address interference fringe effects. Improvements to experimental hardware, such as the introduction of multi-wavelength light sources for spectral imaging will do the same. Nanoscale investigations of the characteristic features of primitive carbonaceous chondrites, especially those like ALH 83100 that is an intermediate between CM1/2 and contains signatures of varying degrees of aqueous alteration, can potentially allow us to better constrain the nebular as well as parent body processes.

Acknowledgments

This work was supported by the RIS^{4}E and RISE2 nodes (T. D. Glotch, PI) of NASA's Solar System Exploration Research Virtual Institute. This research used resources of the Advanced Light Source, a U.S. DOE Office of Science User Facility under contract no. DE-AC02-05CH11231. MY acknowledges support from TUBITAK (projects 119N207 and 120Y115). U.S. Antarctic meteorite samples are recovered by the Antarctic Search for Meteorites (ANSMET) program that has been funded by NSF and NASA, and characterized and curated by the Department of Mineral Sciences of the Smithsonian Institution and Astromaterials Curation Office at NASA Johnson Space Center.

Data Availability Statement

The data collected and used by this work will be stored in a repository at Zenodo.org upon acceptance of the manuscript and will be found by searching for the DOI assigned to this work. Nano-IR spectra are provided for the reviewers as an Excel spreadsheet in Supplementary Information.

References

Alexander, C.M.O.D., Fogel, M., Yabuta, H. and Cody, G.D., 2007. The origin and evolution of chondrites recorded in the elemental and isotopic compositions of their macromolecular organic matter. *Geochimica et Cosmochimica Acta*, *71*(17), 4380-4403.

Alexander, C.M.D., Howard, K.T., Bowden, R. and Fogel, M.L., 2013. The classification of CM and CR chondrites using bulk H, C and N abundances and isotopic compositions. Geochimica et Cosmochimica Acta, 123, pp.244-260.

Amarie, S., Ganz, T. and Keilmann, F. (2009), Mid-infrared near-field spectroscopy. *Optics Express*, *17*(24), 21794-21801.

Amenabar, I., Poly, S., Nuansing, W., Hubrich, E.H., Govyadinov, A.A., Huth, F., Krutokhvostov, R., Zhang, L., Knez, M., Heberle, J. and Bittner, A.M. (2013), Structural analysis and mapping of individual protein complexes by infrared nanospectroscopy. *Nature Communications*, *4*(1), 1-9.

Azarfar, G., Aboualizadeh, E., Walter, N.M., Ratti, S., Olivieri, C., Norici, A., Nasse, M., Kohler, A., Giordano, M. and Hirschmugl, C.J. (2018), Estimating and correcting interference fringes in infrared spectra in infrared hyperspectral imaging. *Analyst*, *143*(19), 4674-4683.

Bates, H. C., A. J. King, K. L. Donaldson Hanna, N. E. Bowles, and S. S. Russell. (2020), "Linking mineralogy and spectroscopy of highly aqueously altered CM and CI carbonaceous chondrites in preparation for primitive asteroid sample return." *Meteoritics & Planetary Science*, *55*(1) 77-101.

Bechtel, H. A., Johnson, S. C., Khatib, O., Muller, E. A., & Raschke, M. B. (2020), Synchrotron infrared nano-spectroscopy and-imaging. *Surface Science Reports*, *75*(3), 100493.

Brearley, A.J., 1990, March. Matrix Mineralogy of the Unequilibrated CO3 Chondrite, ALH A77307: Evidence for Disequilibrium Condensation Processes and Implications for the Origin of Chondrite Matrices. In Lunar and Planetary Science Conference, 21,125.

Brearley, A.J., 1991, March. Subsolidus microstructures and cooling history of pyroxenes in the Zagami shergottite. In Lunar and Planetary Science Conference, 22, 133.

Brearley, A.J. and Geiger, T., 1991. Mineralogical and chemical studies bearing on the origin of accretionary rims in the Murchison CM2 carbonaceous chondrite. Meteoritics, 26, p.323.

Breitenfeld, L. B., A. D. Rogers, T. D. Glotch, V. E. Hamilton, P. R. Christensen, D. S. Lauretta, M. E. Gemma, K. T. Howard, D. S. Ebel, G. Kim, A. M. Kling, H. Nekvasil, and N. J. DiFrancesco (2021), Machine learning mid-infrared spectral models for predicting modal mineralogy of CI/CM chondritic asteroids and Bennu, *J. Geophys. Res.*, 126, e2021JE007035, doi:10.1029/2021JE007035.

Brindley, G. W., J. Zussman. (1959), Infra-red absorption data for serpentine minerals. *American Mineralogist* *44*(1-2): 185–188.

Burns, R.G. and Huggins, F.E.(1972), Cation determinative curves for Mg-Fe-Mn olivines from vibrational spectra. *American Mineralogist: Journal of Earth and Planetary Materials*, *57*(5-6), 967-985.

Clark, R.N. and Roush, T.L. (1984), Reflectance spectroscopy: Quantitative analysis techniques for remote sensing applications. *Journal of Geophysical Research: Solid Earth*, *89*(B7), 6329-6340.

De Leuw, S., Rubin, A.E., Schmitt, A.K. and Wasson, J.T. (2009), *Mn-Cr Systematics for the CM2. 1 Chondrites QUE 93005 and ALH 83100: Implications for the Timing of Aqueous Alteration*. Paper presented at 40th Lunar and Planetary Science Conference, Houston, Texas

de LEUW, S., Rubin, A.E. and Wasson, J.T., 2010. Carbonates in CM chondrites: Complex formational histories and comparison to carbonates in CI chondrites. Meteoritics & Planetary Science, 45(4), pp.513-530.

Dominguez, G., Mcleod, A.S., Gainsforth, Z., Kelly, P., Bechtel, H.A., Keilmann, F., Westphal, A., Thiemens, M. and Basov, D.N. (2014), Nanoscale infrared spectroscopy as a non-destructive probe of extraterrestrial samples. *Nature Communications*, *5*(1), 1-10.

Dorschner, J., Begemann, B., Henning, T., Jaeger, C. and Mutschke, H. (1995), Steps toward interstellar silicate mineralogy. II. Study of Mg-Fe-silicate glasses of variable composition. *Astronomy and Astrophysics*, *300*, 503.

Duke, D.A. and Stephens, J.D. (1964), Infrared investigation of the olivine group minerals. *American Mineralogist: Journal of Earth and Planetary Materials*, *49*(9-10), 1388-1406.

Dürig, U., Pohl, D.W. and Rohner, F. (1986), Near-field optical-scanning microscopy. *Journal of Applied Physics*, *59*(10), 3318-3327.

Dyar, M.D., Sklute, E.C., Menzies, O.N., Bland, P.A., Lindsley, D., Glotch, T., Lane, M.D., Schaefer, M.W., Wopenka, B., Klima, R. and Bishop, J.L. (2009), Spectroscopic characteristics of synthetic olivine: An integrated multi-wavelength and multi-technique approach. *American Mineralogist*, *94*(7), 883-898.

Elsila, J.E., Charnley, S.B., Burton, A.S., Glavin, D.P. and Dworkin, J.P. (2012), Compound-specific carbon, nitrogen, and hydrogen isotopic ratios for amino acids in CM and CR chondrites and their use in evaluating potential formation pathways. *Meteoritics & Planetary Science*, *47*(9), 1517-1536.

Fabian, D., Henning, T., Jäger, C., Mutschke, H., Dorschner, J. and Wehrhan, O. (2001), Steps toward interstellar silicate mineralogy-VI. Dependence of crystalline olivine IR spectra on iron content and particle shape. *Astronomy & Astrophysics*, *378*(1), 228-238.

Farrand, W.H., Wright, S.P., Rogers, A.D. and Glotch, T.D. (2016), Basaltic glass formed from hydrovolcanism and impact processes: Characterization and clues for detection of mode of origin from VNIR through MWIR reflectance and emission spectroscopy. *Icarus*, 275, 16-28.

Farrand, W.H., Wright, S.P., Glotch, T.D., Schröder, C., Sklute, E.C. and Dyar, M.D., 2018. Spectroscopic examinations of hydro-and glaciovolcanic basaltic tuffs: Modes of alteration and relevance for Mars. *Icarus*, *309*, 241-259.

Friedlander, L.R., Glotch, T.D., Bish, D.L., Dyar, M.D., Sharp, T.G., Sklute, E.C. and Michalski, J.R. (2015), Structural and spectroscopic changes to natural nontronite induced by experimental impacts between 10 and 40 GPa. *Journal of Geophysical Research: Planets*, *120*(5), 888-912.

583 Friend, P., Hezel, D.C., Barrat, J.A., Zipfel, J. and Palme, H. (2016), *The Chemical Composition*
584 *of Matrix, Chondrules and Bulk Meteorite of the CM Chondrite Jbilet Winselwan*. Paper
585 presented at the 47th Lunar and Planetary Science Conference.

586 Fuente, E., Menéndez, J.A., Díez, M.A., Suárez, D. and Montes-Morán, M.A. (2003), Infrared
587 spectroscopy of carbon materials: a quantum chemical study of model compounds. The Journal
588 of physical chemistry B, *107*(26), 6350-6359.

589 Gillespie, A. R., A. B. Kahle, and R. E. Walker (1986), Color enhancement of highly correlated
590 images. 1. Decorrelation and His contrast stretches, *Remote Sens. Environ.*, 20(3), 209–235,
591 doi:10.1016/0034-4257(86)90044-1.

592 Glotch, T.D., Young, J.M., Yao, Z., Bechtel, H.A., Hamilton, V.E., Christensen, P.R. and Lauretta,
593 D.S., 2019. Near-Field Infrared Spectroscopy as a Tool for Analysis of Chondritic Returned
594 Samples. LPI Contributions, 2189, p.2061.

595 Hamilton, V.E. (2000), Thermal infrared emission spectroscopy of the pyroxene mineral
596 series. *Journal of Geophysical Research: Planets*, *105*(E4), 9701-9716.

597 Hamilton, V.E. (2010), Thermal infrared (vibrational) spectroscopy of Mg–Fe olivines: A review
598 and applications to determining the composition of planetary surfaces. *Geochemistry*, *70*(1),
599 7-33.

600 Hamilton, V.E., Simon, A.A., Christensen, P.R., Reuter, D.C., Clark, B.E., Barucci, M.A., Bowles,
601 N.E., Boynton, W.V., Brucato, J.R., Cloutis, E.A. and Connolly, H.C. (2019), Evidence for
602 widespread hydrated minerals on asteroid (101955) Bennu. *Nature Astronomy*, *3*(4), 332-340.

603 Hamilton, V.E., Haberle, C.W. and Mayerhöfer, T.G., 2020. Effects of small crystallite size on the
604 thermal infrared (vibrational) spectra of minerals. American Mineralogist: Journal of Earth and
605 Planetary Materials, 105(11), pp.1756-1760.

606 Hamilton, V.E., Christensen, P.R., Kaplan, H.H., Haberle, C.W., Rogers, A.D., Glotch, T.D.,
607 Breitenfeld, L.B., Goodrich, C.A., Schrader, D.L., McCoy, T.J. and Lantz, C., 2021. Evidence
608 for limited compositional and particle size variation on asteroid (101955) Bennu from thermal
609 infrared spectroscopy. Astronomy & Astrophysics, 650, p.A120.

610 Donaldson Hanna, K., Schrader, D.L., Cloutis, E.A., Cody, G.D., King, A.J., McCoy, T.J., Applin,
611 D.M., Mann, J.P., Bowles, N.E., Brucato, J.R. Connolly Jr, H.C., Dotto, E., Keller, L.P., Lim,
612 L.F., Clark, B.E., Hamilton, V.E., Lantz, C., Lauretta, D.S., Russell, S.S., and Schofield, P.F.
613 (2019). Spectral characterization of analog samples in anticipation of OSIRIS-REx's arrival at
614 Bennu: A blind test study. *Icarus*, *319*, pp.701-723.

615 Hapke, B. (1981), Bidirectional reflectance spectroscopy: 1. Theory. *Journal of Geophysical*
616 *Research: Solid Earth*, *86*(B4), 3039-3054.

617 Hillenbrand, R. and Keilmann, F. (2000), Complex optical constants on a subwavelength
618 scale. *Physical Review Letters*, *85*(14), 3029.

619 Howard, K.T., Benedix, G.K., Bland, P.A. and Cressey, G. (2011), Modal mineralogy of CM
620 chondrites by X-ray diffraction (PSD-XRD): Part 2. Degree, nature and settings of aqueous
621 alteration. *Geochimica et Cosmochimica Acta*, *75*(10), 2735-2751.

622 Hunt, G.R. and Salisbury, J.W. (1970), Visible and near infrared spectra of minerals and rocks. I.
623 Silicates. *Modern Geology*, *2*, 23-30.

Jaret, S.J., Woerner, W.R., Phillips, B.L., Ehm, L., Nekvasil, H., Wright, S.P. and Glotch, T.D. (2015), Maskelynite formation via solid-state transformation: Evidence of infrared and X-ray anisotropy. *Journal of Geophysical Research: Planets*, *120*(3), 570-587.

Jaret, S.J., Johnson, J.R., Sims, M., DiFrancesco, N. and Glotch, T.D. (2018). Microspectroscopic and petrographic comparison of experimentally shocked albite, andesine, and bytownite. *Journal of Geophysical Research: Planets*, *123*(7), pp.1701-1722.

Johnson, P.E., Smith, M.O., Taylor-George, S. and Adams, J.B. (1983), A semiempirical method for analysis of the reflectance spectra of binary mineral mixtures. *Journal of Geophysical Research: Solid Earth*, *88*(B4), 3557-3561.

Johnson, J.R., Jaret, S.J., Glotch, T.D. and Sims, M., 2020. Raman and infrared microspectroscopy of experimentally shocked basalts. *Journal of Geophysical Research: Planets*, *125*(2),

Kaplan, H.H., Lauretta, D.S., Simon, A.A., Hamilton, V.E., DellaGiustina, D.N., Golish, D.R., Reuter, D.C., Bennett, C.A., Burke, K.N., Campins, H. and Connolly, H.C., 2020. Bright carbonate veins on asteroid (101955) Bennu: Implications for aqueous alteration history. *Science*, *370*(6517)

Kebukawa, Y., Kobayashi, H., Urayama, N., Baden, N., Kondo, M., Zolensky, M.E. and Kobayashi, K. (2019), Nanoscale infrared imaging analysis of carbonaceous chondrites to understand organic-mineral interactions during aqueous alteration. *Proceedings of the National Academy of Sciences*, *116*(3), 753-758.

Kereszturi, A., Blumberger, Z., Józsa, S., May, Z., Müller, A., Szabó, M. and Tóth, M. (2014). Alteration processes in the CV chondrite parent body based on analysis of NWA 2086 meteorite. *Meteoritics & Planetary Science*, *49*(8), 1350-1364.

Kereszturi, A., Gyollai, I. and Szabó, M., (2015). Case study of chondrule alteration with IR spectroscopy in NWA 2086 CV3 meteorite. *Planetary and Space Science*, *106*, 122-131.

King, T.V. and Ridley, W.I. (1987), Relation of the spectroscopic reflectance of olivine to mineral chemistry and some remote sensing implications. Journal of Geophysical Research: Solid Earth, *92*(B11), 11457-11469.

King, A.J., Solomon, J.R., Schofield, P.F. and Russell, S.S. (2015) Characterising the CI and CI-like carbonaceous chondrites using thermogravimetric analysis and infrared spectroscopy. *Earth, Planets and Space*, 67(1), 1-12.

Kitazato, K., Milliken, R.E., Iwata, T., Abe, M., Ohtake, M., Matsuura, S., Arai, T., Nakauchi, Y., Nakamura, T., Matsuoka, M. and Senshu, H. (2019), The surface composition of asteroid 162173 Ryugu from Hayabusa2 near-infrared spectroscopy. *Science*, *364*(6437), 272-275.

Labardi, M., Patane, S. and Allegrini, M. (2000), Artifact-free near-field optical imaging by apertureless microscopy. *Applied Physics Letters*, *77*(5), 621-623.

Lane, M.D., T.D. Glotch, M.D. Dyar, C.M. Pieters, R. Klima, T. Hiroi, J.L. Bishop, and J. Sunshine. (2011), "Midinfrared spectroscopy of synthetic olivines: Thermal emission, specular and diffuse reflectance, and attenuated total reflectance studies of forsterite to fayalite." *Journal of Geophysical Research: Planets 116*(E8)

Lauretta, D.S., DellaGiustina, D.N., Bennett, C.A., Golish, D.R., Becker, K.J., Balram-Knutson, S.S., Barnouin, O.S., Becker, T.L., Bottke, W.F., Boynton, W.V. and Campins, H. (2019), The unexpected surface of asteroid (101955) Bennu. *Nature*, *568*(7750), 55-60.

Lindgren, P., Lee, M.R., Sparkes, R., Greenwood, R.C., Hanna, R.D., Franchi, I.A., King, A.J., Floyd, C., Martin, P.E., Hamilton, V.E. and Haberle, C. (2020), Signatures of the post-hydration heating of highly aqueously altered CM carbonaceous chondrites and implications for interpreting asteroid sample returns. *Geochimica et Cosmochimica Acta*, *289*, 69-92.

Mayerhöfer, T.G., Pahlow, S., Hübner, U. and Popp, J. (2018), Removing interference-based effects from the infrared transflectance spectra of thin films on metallic substrates: a fast and wave optics conform solution. *Analyst*, *143*(13), 3164-3175.

Mustard, J.F. and Pieters, C.M. (1987), Quantitative abundance estimates from bidirectional reflectance measurements. *Journal of Geophysical Research: Solid Earth*, *92*(B4), 617-626.

Nasse, M.J., Walsh, M.J., Mattson, E.C., Reininger, R., Kajdacsy-Balla, A., Macias, V., Bhargava, R. and Hirschmugl, C.J., 2011. High-resolution Fourier-transform infrared chemical imaging with multiple synchrotron beams. Nature methods, 8(5), pp.413-416.

Orthous-Daunay, F.R., Quirico, E., Beck, P., Brissaud, O., Dartois, E., Pino, T. and Schmitt, B. (2013), Mid-infrared study of the molecular structure variability of insoluble organic matter from primitive chondrites. *Icarus*, *223*(1), 534-543.

Palme, H., Hezel, D. C., & Ebel, D. S. (2015). The origin of chondrules: Constraints from matrix composition and matrix-chondrule complementarity. *Earth and Planetary Science Letters*, *411*, 11-19.

Pearson, V.K., Sephton, M.A., Kearsley, A.T., Bland, P.A., Franchi, I.A. and Gilmour, I. (2002), Clay mineral-organic matter relationships in the early solar system. *Meteoritics & Planetary Science*, *37*(12), 1829-1833.

Reynard, B. (1991), Single-crystal infrared reflectivity of pure Mg_2SiO_2 forsterite and $(Mg_{0.86}, Fe_{0.14})_2SiO_4$ olivine. *Physics and Chemistry of Minerals*, *18*(1), 19-25.

Shirley, K.A. and Glotch, T.D. (2019), Particle size effects on mid-infrared spectra of lunar analog minerals in a simulated lunar environment. *Journal of Geophysical Research: Planets*, *124*(4), 970-988.

Simon, A.A., Kaplan, H.H., Hamilton, V.E., Lauretta, D.S., Campins, H., Emery, J.P., Barucci, M.A., DellaGiustina, D.N., Reuter, D.C., Sandford, S.A. and Golish, D.R. (2020), Widespread carbon-bearing materials on near-Earth asteroid (101955) Bennu. *Science*, *370*(6517).

Takir, D., Emery, J.P., Mcsween Jr, H.Y., Hibbitts, C.A., Clark, R.N., Pearson, N. and Wang, A. (2013), Nature and degree of aqueous alteration in CM and CI carbonaceous chondrites. *Meteoritics & Planetary Science*, *48*(9), 1618-1637.

Teolis, B.D., Loeffler, M.J., Raut, U., Famá, M. and Baragiola, R.A. (2007), Infrared reflectance spectroscopy on thin films: Interference effects. *Icarus*, *190*(1), 274-279.

Velbel, M.A. and Palmer, E.E. (2011), Fine-grained serpentine in CM2 carbonaceous chondrites and its implications for the extent of aqueous alteration on the parent body: A review. *Clays and Clay Minerals*, *59*(4), 416-432.

Xu, X.G., Rang, M., Craig, I.M. and Raschke, M.B. (2012), Pushing the sample-size limit of infrared vibrational nanospectroscopy: from monolayer toward single molecule sensitivity. *The Journal of Physical Chemistry Letters*, *3*(13), 1836-1841.

Yesiltas, M., Hirschmugl, C.J. and Peale, R.E., 2013. In situ investigation of meteoritic organic-mineral relationships by high spatial resolution infrared spectroscopy. Meteoritics and Planetary Science Supplement, 76, p.5068.

Yesiltas, M. and Kebukawa, Y. (2016), Associations of organic matter with minerals in Tagish Lake meteorite via high spatial resolution synchrotron-based FTIR microspectroscopy. *Meteoritics & Planetary Science*, *51*(3), 584-595.

Yesiltas, M., Sedlmair, J., Peale, R.E. and Hirschmugl, C.J., 2017. Synchrotron-based three-dimensional Fourier-transform infrared spectro-microtomography of Murchison meteorite grain. Applied spectroscopy, 71(6), pp.1198-1208.

Yesiltas, M., Kaya, M., Glotch, T.D., Brunetto, R., Maturilli, A., Helbert, J. and Ozel, M.E. (2020), Biconical reflectance, micro-Raman, and nano-FTIR spectroscopy of the Didim (H3-5) meteorite: Chemical content and molecular variations. *Meteoritics & Planetary Science*, *55*(11), 2404-2421.

Yesiltas, M., T. D. Glotch, and B. Sava (2021), Nano-FTIR spectroscopic identification of prebiotic carbonyl compounds in Dominion Range 08006 carbonaceous chondrite, *Scientific Reports*, 11, 11656, doi:10.1038/s41598-021-91200-8.

Zega, T.J. and Buseck, P.R. (2003), Fine-grained-rim mineralogy of the Cold Bokkeveld CM chondrite. *Geochimica et Cosmochimica Acta*, *67*(9), 1711-1721

Zega, T.J., Garvie, L.A., Dódony, I., Friedrich, H., Stroud, R.M. and Buseck, P.R. (2006), Polyhedral serpentine grains in CM chondrites. *Meteoritics & Planetary Science*, *41*(5), 681-688.

Zolensky, M., Barrett, R. and Browning, L. (1993), Mineralogy and composition of matrix and chondrule rims in carbonaceous chondrites. *Geochimica et Cosmochimica Acta*, *57*(13), 3123-3148.

Zolensky, M.E., Mittlefehldt, D.W., Lipschutz, M.E., Wang, M.S., Clayton, R.N., Mayeda, T.K., Grady, M.M., Pillinger, C. and David, B., 1997. CM chondrites exhibit the complete petrologic range from type 2 to 1. Geochimica et Cosmochimica Acta, 61(23), pp.5099-5115.